International Journal of Biological Macromolecules 163 (2020) 730–744

Contents lists available at ScienceDirect

International Journal of Biological Macromolecules

journal homepage: http://www.elsevier.com/locate/ijbiomac

Mapping the underlying mechanisms of fibrinogen benzothiazole drug interactions using computational and experimental approaches

Michael González-Durruthy [a,b], Gustavo Scanavachi [c], Ramón Rial [a], Zhen Liu [d], M. Natália D.S. Cordeiro [b], Rosangela Itri [c], Juan M. Ruso [a,*]

[a] Soft Matter and Molecular Biophysics Group, Department of Applied Physics, University of Santiago de Compostela, 15782 Santiago de Compostela, Spain
[b] LAQV@REQUIMTE/Department of Chemistry and Biochemistry, Faculty of Sciences, University of Porto, 4169-007 Porto, Portugal
[c] Department of Applied Physics, Institute of Physics, University of São Paulo, 05508-090 São Paulo, Brazil
[d] Department of Physics and Engineering, Frostburg State University, Frostburg, MD 21532, United States

ARTICLE INFO

Article history:
Received 30 April 2020
Received in revised form 16 June 2020
Accepted 6 July 2020
Available online 9 July 2020

Keywords:
Fibrinogen
BTS
Molecular docking
2D-FFT signals
Fractal analysis

ABSTRACT

Three-dimensional conformational crystallographic binding-modes are of paramount importance to understand the docking mechanism of protein-ligand interactions and to identify potential "*leading drugs*" conformers towards rational drugs-design. Herein, we present an integrated computational-experimental study tackling the problem of multiple binding modes among the ligand 3-(2-Benzothiazolylthio)-propane sulfonic acid (BTS) and the fibrinogen receptor (E-region). Based on molecular docking simulations, we found that the free energy of binding values for nine of different BTS-docking complexes (*i.e.*, BTS-*pose_1–9*) were very close. We have also identified a docking-mechanism of BTS-interaction mainly based on non-covalent hydrophobic interactions with H-bond contacts stabilizing the fibrinogen-BTS docking complexes. Interestingly, the different BTS-*poses_1–9* were found to be able to block the fibrinogen binding site (E-region) by inducing local perturbations in effector and allosteric residues, reducing the degree of collectivity in its flexibility normal modes. As such, we theoretically suggest that the BTS-binding modes can significantly affect the physiological condition of the unoccupied fibrinogen protein structure by bringing global and local perturbations in the frequency domain spectra. The proposed theoretical mechanisms, the interactions involved and the conformational changes suggested, were further corroborated by different experimental techniques such as isothermal titration calorimetry (ITC), zeta potential, UV–vis, fluorescence and small angle X-ray scattering (SAXS). The combined results shall open new avenues towards the application of complex supra-molecular information in rational drugs-design.

1. Introduction

Proteins are responsible for most of the functions that occur in living organism, and for that purpose they need to maintain their three-dimensional structure. However, this is not an easy task because they are thermodynamically active, highly dynamic and tend to interact with several competing targets [1–3]. In this context, the arrangement by which proteins interact with other molecular entities, whether specifically or not, has challenged many [4,5].

Many diseases are based on biomolecular interactions. The different interactions of the proteins trigger mechanisms and signals that can indicate the state of health or disease in the organisms. Thus, protein interactions are behind the molecular basis of diseases and might assist methods of prevention, diagnosis and treatment [6]. On the other hand, the increase in the clinical use of therapeutic proteins has drawn attention to the potential for protein–drug interactions [7] and regulatory agencies have recently issued interaction guidelines, which require determination of plasma protein binding [8].

Fibrinogen (or factor I) is a large and elongated triglobular protein, part of the blood plasma of vertebrates. Its main function is to form fibrin clots to avoid the loss of blood due to injury. The protein (around 340 kDa) is 45 nm long, with a diameter of 5 nm, comprising a round disulfide-linked dimer composed of three pairs of nonidentical polypeptide chains, called Aα, Bβ, and γ (attached with 29 disulfide bonds and no free sulfhydryl groups), the predominant forms of which have 610, 461, and 411 amino acids, respectively [9]. Plasma levels of fibrinogen have been described as risk predictors of cardiovascular disease. It has been shown that drugs such as ticlopidione or fibrates are effective reducing fribrinogen levels. In addition, this effectiveness is affected by various factors, such as the presence of other diseases like diabetes [10]. Curcumin is a popular pigment with numerous known medical applications [11]. However, its rapid degradation in biological fluids limits its action. Leung et al. have shown that the binding of curcumin to fibrinogen suppresses the degradation process by 95% [12]. Further, nanoparticles have been demonstrated to be very important for drug

* Corresponding author.
E-mail address: juanm.ruso@usc.es (J.M. Ruso).

https://doi.org/10.1016/j.ijbiomac.2020.07.044
0141-8130/

delivery systems and, consequently, highlighting the role of protein-nanoparticle interactions [13]. In that respect, the binding of fibrinogen with gold nanoparticles has also been reported, underlining the importance of the process dynamics [14]. Computational techniques have also been focused on fibrinogen. Liu et al. have reported molecular docking simulations of the interaction of an anticoaagulant drug and fibrinogen to obtain features of the possible binding models. They found that hydrogen bonding and hydrophobic interactions embody 86% of the total energy [15].

Benzothiazole derivatives have been extensively applied in both therapeutic treatments and diagnosis including amyloid-β markers and dyes to follow protein conformational changes in cells. It has been discovered that a series of benzothiazoles substitutes are selective and high affinity inhibitors of different triosephosphate isomerases (TIM) including Tripanosome cruzi (Tc) and Tripanosome brucei (Tb) TIMs. Among the anti-tumor drugs discovered recently, several studies have concluded that the benzothiazole nucleus has a strong anticancer activity against human cancers. Some authors have found that some compounds including the benzothiazol nucleus killed cells in a tumor-specific way. Benzothiazoles derivatives have indeed been reported to possess potent anticancer properties due to their structural similarity with naturally occurring purines as they can easily interact with biomolecules of the living systems [16]. Diverse biological activities such as antiviral, antifungal or antibacterial have also been described [17,18].

In this light, this work aims at disclosing the interactions between fibrinogen and 3-(2-Benzothiazolylthio)-propanesulfonic acid (BTS). In order to establish different approaches and strategies to deal with this system, emphasis has been placed on innovative approaches. Thus, molecular docking and local perturbation response scanning maps were chosen, since these give information about the interaction energy and local protein conformational changes [19,20]. Further, we introduce for the first time, a combined methodology by using two recognized image-processing algorithms to tackle the ligand-conformations problem of BTS from a qualitative and quantitative point of view, namely: Fast Fourier transform (2D-FFT) and fractal approaches [21,22]. These two methods offered information about the supramolecular complex. On the other hand, experimental results provided by isothermal titration calorimetry, UV–Vis, fluorescence, zeta potential and Small Angle X-ray scattering were analyzed and contrasted with the computational ones.

2. Material and methods

2.1. Materials

Bovine plasma fibrinogen, fraction I, type IV, was obtained from Sigma (No. 9001-32-5). 3-(2-Benzothiazolylthio)-propanesulfonic acid (BTS) (>97% purity) was purchased from Aldrich Lancaster. The buffer solution used for fibrinogen was 50 mN glycine plus sodium hydroxide to give a pH of 8.5 (fibrinogen will be negatively charged). Samples were prepared within 1 h prior to usage. All chemical reagents were of analytical grade, and solutions were made using doubly distilled and degassed water.

2.2. Experimental methods

2.2.1. Isothermal titration calorimetry

Experiments were carried out in a VP-ITC microcalorimeter (MicroCal Inc., Northampton, U.S.) [23]. In order to determine the binding isotherms, the drug solution 1 mM were introduced into the syringe (296 μL), while the fibrinogen solution 0.033 mM were introduced into the sample cell (1.4166 mL). The stirring was kept constant at 416 rpm. An important factor to take into account is the equilibrium time necessary before starting each experiment, in our case it was 1 h, more than enough for the power base line to remain stable. 28 injections of 5 μL at a constant rate of 0.5 μL s^{-1} plus a first one of 2 μL were introduced in the cell every 300 s. To eliminate negative signals, a reference power of 25 μJ s^{-1} was applied. Thus, it is guaranteed that the signal is not altered by any overcompensation mechanism. Dilution experiments of pure drugs were also conducted. The values obtained were systematically subtracted from those measured for the fibrinogen-drug systems. In this way, it is guaranteed that all the heat produced in the cell is due solely to the binding process. Following the described procedure, experiments were performed at a temperature of 298.15 K.

2.2.2. Zeta potential

A Malvern Zeta Sizer Nano (ZS90) with a He-Ne laser (λ = 633 nm) was used. Malvern's software provides the zeta potential from electrophoretic mobilities using the Henry equation [19].

2.2.3. UV–vis absorption spectra

The UV–vis absorption measurements were recorded with a Cary 100 Bio UV–Vis Spectrophotometer. The investigated spectral range was 250–450 nm. The BTS concentration used was 20 μM and the working temperature was maintained constant at 298.15 K.

2.2.4. Fluorescence measurements

A Cary Eclipse spectrofluorimeter was used to perform the fluorescence measurements. The emission and excitation splits were 5 nm. The data interval was set to 1 nm and the averaging time at 0,5 s. The synchronous fluorescence spectra of fibrinogen due to the presence of the aromatic residues were obtained within a range of 290–450 nm upon excitation at 280 nm. The temperature was fixed at 298.15 K maintaining the Fibrinogen concentration constant at 1 μM, and increasing concentrations of BTS from 0 μM to 200 μM. (1, 2, 4,8, 10, 50, 100, 200 μM). In order to avoid unreliable results, the inner filter effects were corrected for the fluorescence quenching data as follows: $F_{corrected} = F_{observed}\, e^{(A_{excitation}+A_{emission})}$; where, $F_{corrected}$ and $F_{observed}$ are the corrected and observed fluorescence intensities and $A_{excitation}$ and $A_{emission}$ are the absorption of the systems at the excitation and the emission wavelength, respectively. UV–Vis-IR Spectral Software from FluorTools was used for data processing [24,25].

2.2.5. SAXS acquisition and data analysis

SAXS experiments were carried out at SAXS beamline from the National Synchrotron Light Laboratory (LNLS) Campinas, Brazil. SAXS experiments from BTS at concentrations of 70, 110, 150 or 180 mM (cmc around 170 mM, at pH 5.5 at room temperature [26]) were taken in the absence and presence of 0.5 mg/mL of fibrinogen-containing buffer solution (50 mM glycine at pH 8.5). SAXS curve from 0.5 mg/mL of fibrinogen was also obtained. Samples were placed perpendicular to the incoming X-Ray beam (wavelength λ = 1.488 Å) in between a mica window. The scattered X-Ray data were recorded by a 2D Pilatus detector in the q interval ranging from 0.012 $Å^{-1}$ to 0.45 $Å^{-1}$, where q is the scattering vector ($q = (4\pi/\lambda)\sin\theta$ with 2θ the scattering angle). All measurements were performed at room temperature of 298 K.

The scattering intensity $I(q)$ is related to the scattering particle form factor, $P(q)$, and structure factor, $S(q)$, as described by

$$I(q) = kn_pP(q)S(q) \quad (1)$$

where k is an instrumental parameter and n_p is the scattering particle number density [27]. In particular, the drug-free fibrinogen solution was previously analyzed considering that the whole scattering was due to a linear combination of two species coexisting in solution: paired-dimer and dimer of the fibrinogen (PDB id: 3GHG [28]) [29], with no correlation between them such that $S(q) = 1$. The result pointed out the coexistence of 63% of the paired-dimers and 37% of the fibrinogen dimers [29].

The SAXS curves from BTS solutions were analyzed through pair distribution functions, $p(r)$, to infer about the formation of self-assembled

BTS [30]. The $p(r)$ functions were calculated using the GNOM software [31].

A qualitative analysis of the SAXS curves from fibrinogen in the presence of a given BTS concentration was done by comparing the experimental data with the expected ones considered as a linear combination of the individual scatterings from the fibrinogen and BTS in solution.

2.3. Computational approaches

2.3.1. Computational modeling-based molecular docking

To study the binding properties between BTS and fibrinogen protein (E-region) a theoretical mechanistic study based on molecular docking was performed. Towards such end, first we prepared the protein receptor file (*i.e.*, fibrinogen E-region), which was withdrawan from the *RCSB Protein Data Bank* (PDB) X-ray structures [32], *i.e.* with *PDB ID*: 1JY2. Afterwards, the fibrinogen (E-region) receptor molecular structure was optimized by applying the AutoDock Tools 4 software, using the AutoDock Vina scoring function [33,34]. This software starts by removing all the crystallographic waters as well as all co-crystallized ligands if present. Next, H-atoms were included in the fibrinogen protein structure, following an appropriate hybridization geometry by adding Gasteiger-Marsili empirical atomic partial-charges and protonation states of the X-ray fibrinogen pdb structure [33]. Following this, the BTS ligand was obtained from the *Pubchem Data Base Chemical Structure Search* (PubChem CID: 162569; MF: $C_{10}H_{11}NO_3S_3$). The drug geometry optimization was carried out by using the MOPAC extension based on NDDO approximation [35]. To study the drug docking mechanisms with bovine fibrinogen E-region, we used the Autodock Vina scoring function developed by Trott et al. [33] to obtain the free energy of binging (FEB) based on X-Score function which approximates the standard chemical potentials. Before the docking modeling, the fibrinogen E-region binding-sites were predicted through the ezPocket with *fconv* for binding-site detection [36–38]. This step was carried out as delimiting the access to fibrinogen-cavities, like van der Waals surfaces that are likely to bind to the ligands (BTS). To this end, the *fconv* analysis uses Delaunay triangulation with weighted points to detect plausible binding pockets. Herein, the volumetric map of the fibrinogen binding-site is generated together with the Cartesian *XYZ*-coordinates for the docking box simulations [39], *i.e.*: grid box size with dimensions of X = 64 Å, Y = 52 Å, Z = 52 Å and grid box center X = 13.1 Å, Y = −2.0 Å, Z = 12.5 Å. For this purpose, a docking accuracy was fixed at 100 and after that, the best nine conformations or BTS binding-poses were selected [34]. The docking affinity (FEB values) were classified like energetically-unfavorable when the FEB of fibrinogen-BTS complexes ≥0 kcal/mol, therefore indicating either extremely low or complete absence of affinity; otherwise the fibrinogen-BTS docking complexes were classified like medium to high docking affinity [36].

2.3.2. 3D Lig-Plot diagrams

This algorithm was applied to evaluate the influence in the FEB values for the different contributions of the ligand binding-poses (BTS binding-poses = 9) interacting with the fibrinogen E-region. To specified the key relevant intermolecular interactions between BTS binding-poses with the fibrinogen, 3D Lig-Plot diagrams were analyzed. To tackle this objective, a software named ezLigPlot was used. This software determines the non-covalent intermolecular interactions present in a given protein-ligand complex and it builds automatically a 3D-interaction diagram that includes hydrophobic, H-bond, cation-Π, and Π-Π stacking interactions along with its corresponding interatomic distances (d_{ij}) for each BTS binding-poses from the obtained docking complexes [40].

2.3.3. Perturbation response maps and collectivity degree-based elastic network models

This computational approach evaluates the degree of change (*i.e.*, interatomic distances perturbation between residue fluctuations) induced by a given ligand (BTS) in the residues network (fibrinogen E-region) by describing the receptor-ligand complex ($fib_{(j)}$-$Lig_{(i)}$ *or R-L*) interaction potential (U) as a Hookean potential based on an elastic network analysis (ENM) [20]. Herein, the perturbation response-induced by BTS on fibrinogen binding-site was estimated by averaging across all the fibrinogen binding-residues for different amplitudes between the perturbed and the unperturbed state of the displacements from equilibrium using anisotropic vibrational analysis [41]. That is, using the following equation:

$$e_{p_{(i)}} = \frac{1}{N_a}\sum_{j=1}^{N_a} |p_j - u_j| \tag{2}$$

where $e_{p(i)}$ stands for the effect of the perturbation response in the anisotropic normal mode (i), p_j is the displacement of the fibrinogen E-region residue (j) in the perturbed normal mode ($(d_{ij} - d_{ij}^0)^2_{\text{R-L}}$), u_j stands for the displacement of individual fibrinogen interacting residues (j) in the unperturbed normal mode ($(d_{ij} - d_{ij}^0)^2_{\text{R-R}}$), and N_a is the number of binding site residues obtained from the 3D Lig-Plot diagram analysis of each BTS binding-poses in the fibrinogen E-region protein receptor. The $e_{p(i)}$ effect is depicted as a local perturbation response scanning map (LPRS map) for the different BTS binding-poses. Here the i^{th} rows are related to the response generated upon perturbing fibrinogen residue (i) and its average (*i.e.*, over all k-receivers residues of fibrinogen). While the k^{th} columns of the LPRS maps depict the sensitivity in response to the perturbation for all the fibrinogen allosteric residues (j-sensors residues) [42]. We also consider other recognized parameters, like the degree of collectivity (K) for a given k-normal mode. This biophysical parameter informs about how the structural elements (fibrinogen binding residues) move together in that particular mode (k). Then, $K(k)$ is useful to estimate the cooperativity degree between residues in a given k-normal mode as shown below.

$$K_{k(R-L)} = \frac{1}{N} e^{-\sum_i^N (\Delta d_{ij})^2} \ln(\Delta d_{ij})^2 \tag{3}$$

where k is the normal mode number, Δd_{ij} ($= d_{ij} - d_{ij}^0$) stands for the amplitude of the individual displacement induced by the different BTS-ligand binding poses (*i.e.*, displacements from R-L perturbation) as previously defined [43,44].

2.3.4. LPRS-maps image analysis-based on Fractal and Fast Fourier Transform

Herein, we introduced for the first time a combination of *Fast Fourier Transform* (2D-FFT) and two fractal approaches - that is, Mandelbrot set and box-counting methods [45,46], in order to identify different perturbation signals and fractal patterns based on local geometrical perturbations from the computational image processing. Those images were obtained from the LPRS maps for the different BTS-binding poses interacting with the fibrinogen E-region. For this purpose, we applied digital image processing based on 2D-Fast Fourier Transform (2D-FFT) for the previously obtained unperturbed and perturbed fibrinogen LPRS-maps. The FFT algorithm is a powerful digital image processing tool, which is used to decompose an image (LPRS maps) into its *sine* and *cosine* components. The number of frequencies ($\omega = 2\pi kn/N$) corresponds to the number of pixels (N) in the original LPRS map image (input image). These calculated frequencies contain relevant information about the geometric pattern of the biological response [47,48]. This fact allows the identification of spatiotemporal properties and patterns of complex pharmacological systems, such as the ones here targeted, *i.e.* the BTS-ligand binding conformations in the fibrinogen protein receptor. More details on this modeling algorithms will be

discussed in the next section. Following the same objective, we apply the computational LPRS maps image modeling based on Mandelbrot set (or ***M***), and found to exhibit an infinitely complicated boundary that shows progressively ever-finer recursive details according to the increasing image magnifications [49]. The geometry shape of this repeating detail depends on the region of the set being studied in the LPRS maps. The Mandelbrot set is formed for an infinite number of distorted copies of itself and the central region of any of these copies represents an approximate cardioid. These cardioids structures are generated by the rolling trajectory described by a point (which represents a given perturbed or unperturbed fibrinogen-residue) included inside a *circle 1* around a fixed *circle 2* with the same radius. In addition, the Mandelbrot set is linked to a Julia set, which generates self-similarly complex geometries based on fractal shapes [50]. To generate the Mandelbrot set images for the different LPRS maps of BTS-ligand binding modes, we used the GNU Image Manipulation Program_GIMP software. By the other hand, we applied the *Box counting method*, carried out by sampling image-data like fractal dimensions (FDs by computing the number of binary black (B) and white (W) pixels or boxes representing different types of FD, namely: D_{BW}, D_{BBW} and D_{WBW} [51,52]).

3. Results and discussion

3.1. Molecular docking and 3D Lig-Plot diagrams by BTS-binding poses

An important step to ensure accuracy of our theoretical approach is the identification/prediction of feasible binding-sites in the receptor protein molecule [53,54]. In the present study the prediction of fibrinogen-binding sites was performed by using an *ezPocket* tool with maximum score equal to 1.0 for the fibrinogen molecule. This binding pocket detection algorithm works with a consensus approach using the *fconv* method [36,37] which is based on Delaunay triangulation to detect plausible fibrinogen binding pockets, typically taking a few seconds with accurate Cartesian *XYZ*-coordinates for the docking box simulations. In our case, this modeling task acquires a paramount importance because we tackle the docking study with a single molecule (BTS). The different binding-conformations that BTS can adopt into the fibrinogen-binding site can significantly influence its Gibbs free energy of binding (FEB) following two criteria: 1) by inducing a little studied phenomenon so-called *intrinsic ligand-promiscuity* [55,56] according to the number of evaluated conformations in the same biophysical environment of a given protein receptor and 2) attributable to the proteins having at least one similar binding-cavity that could, in principle, accommodate small ligands in different conformations. Based on this, we can suggest that the simultaneous modulation of several target residues (effector and allosteric residues) by means of one single BTS molecule can be evaluated in a robust and unequivocal way and also with different types of non-covalent docking interactions, such as hydrophobic, H-bond, cation-Π, and Π-Π stacking interactions with its corresponding interatomic distances (d_{ij}) for each BTS binding-poses from the obtained docking complexes [57]. Figs. 1 and SM1 (the latter shown in the Supporting Information - SI) illustrate and compare the different BTS binding-poses.

It is important to note that, the formation of the docking complexes follows a spontaneous thermodynamic process (FEB < 0 kcal/mol) for the nine conformations evaluated with a high prevalence of hydrophobic interactions in most cases and with different patterns of interacting fibrinogen residues. By the other hand, the presence of H-bond contacts contributes to the stabilization of the formed BTS-fibrinogen complexes, but these were only identified for the BTS_*pose 1* (FEB = −7.0 kcal/mol), BTS_*pose 2* (FEB = −6.8 kcal/mol), BTS_*pose 4* (FEB = −4.8 kcal/mol), and the BTS_*pose 5* (FEB = −4.7 kcal/mol), which in turn present the most negative FEB values of interactions according to more stable docking complexes.

3.2. Perturbation response maps and collectivity degree by BTS-ligand conformation

Let us now discuss the relationships between the different BTS-docking poses, their ability to induce local-perturbations in the fibrinogen residue network, and the change in the collectivity degree [58,59]. The local perturbation response scanning maps (LPRS-maps) show the different patterns of perturbation (interactions) with the fibrinogen E-region target-residues in the absence (unoccupied fibrinogen E-region) and presence of different conformations adopted by BTS. Given a protein, it is well-known that vibration modes between its residue pairs can be affected by the presence of ligands due to changes induced by residues' distance fluctuations and deformation energy effects [20,60,61]. In fact, the transitions between the functional states in the fibrinogen E-region binding-site are strongly dependent on the fibrinogen flexibility properties owing to the presence of allosteric intercommunications between cluster of residues. In this respect, we theoretically suggest that, the different BTS_*poses* evaluated can directly affect the residue network topology (*i.e.* the interaction matrix) for effector (i) and allosteric residues (j) of the fibrinogen binding-site. The results obtained from this perturbation response analysis are illustrated in Figs. 2 and SM2 (SI). The i^{th} rows LPRS-maps are linked to the effector response triggered upon perturbing residue (i) and to its average (*i.e.*, over all receiver residues of fibrinogen). Likewise, the k^{th}-columns of the LPRS-maps show the sensitivity in response to the perturbation induced by BTS-ligand poses in all the fibrinogen allosteric residues (j-sensors residues).

Based on these LPRS maps, we found several differences on the behavior of the biophysical parameter collectivity degree $K(k)$ [59]. That is, in general terms, we discovered a slight tendency to decrease when we compare the $K(k)$ values for the case of BTS-binding poses (BTS_*pose 3–5*), which are around ~0.5 in the normal mode 2 (Figs. 3 and SM3), with the ones for the unoccupied fibrinogen E-region. A high $K(k)$ value is frequently associated to high entropy, which means that highly cooperative normal modes are influenced by a significant region or domain in the protein structure, *i.e.*, the ligands show to induce perturbations with motion fluctuations distributed over a larger number of residues that can be extended to the full protein. From the biophysical point of view, a higher $K(k)$ can trigger cooperative allosteric responses that are linked to lower frequency of motion of the protein. This is mainly of interest to explain the protein dynamics and physiological functions when the changes in docking free energy (FEB values) are imperceptible [60] like those induced by the different binding-conformation (BTS_poses *1–9*) with respect to the reference simulation condition - unoccupied fibrinogen E-region used as control experiment.

3.3. Fourier transform based on BTS-ligand conformational analysis

Herein, we applied 2D-FFT approach to explain non-trivial interaction patterns based on the different conformations of BTS ligand with the fibrinogen protein receptor [21,62]. To do so, we gather the individual profiles coming from the 2D-FFT analysis of the nine conformations adopted by the BTS ligand in the fibrinogen E-region binding-site, and resulting from the computational image processing of the local perturbation response maps of BTS-ligand conformations. The results of this approach are presented in Fig. 4.

Specifically, the LPRS-map images were decomposed to a linear combination of two harmonic orthogonal functions to obtain the symmetric 2D-FFT spectrum, in which the lowest frequency (*i.e.*, the average pixel values) is depicted near the center [0,0], whereas the highest one can be detected near the corner of the 2D-FFT spectrum. The differences between the 2D-FFT patterns obtained from each BTS-ligand conformation are established by the direction of the lines in the spectra, which in turn are defined by the direction of the 2D-spatial sinusoids. For the BTS-binding poses up to 9, we show the 2D-FFT frequency spectra coming from the filtration of 2D-perturbation signals of the

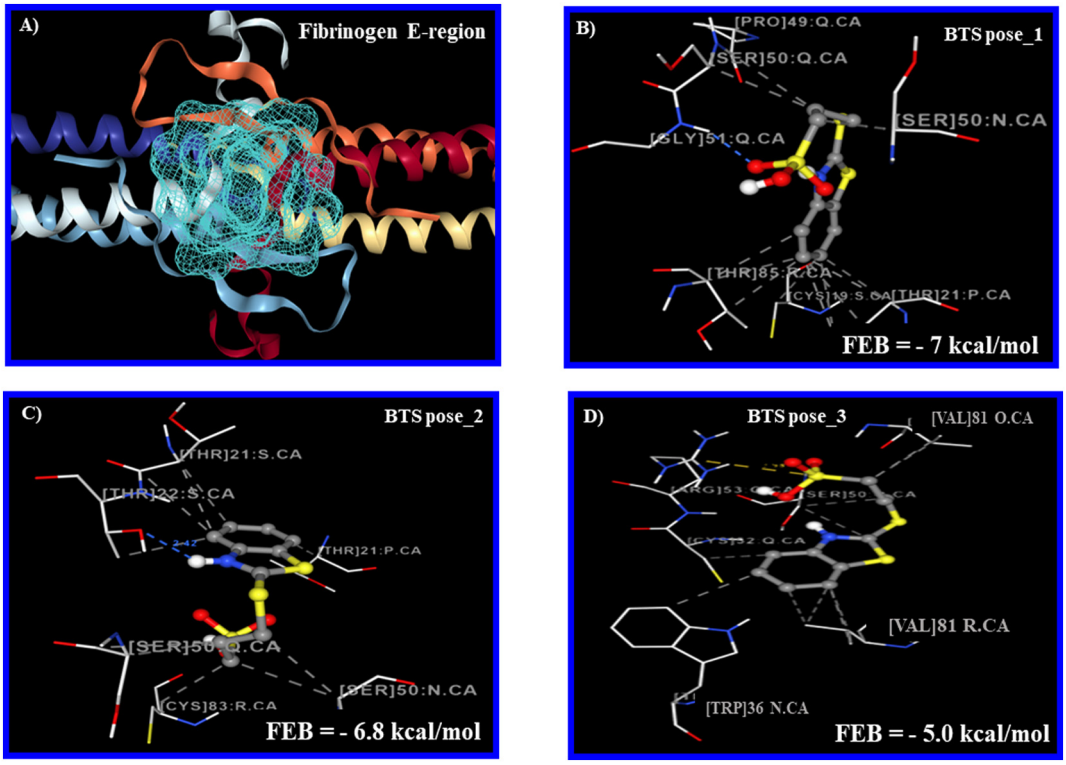

Fig. 1. Results of molecular docking simulation between BTS_binding poses and fibrinogen E-region. A) Theoretical prediction of the main fibrinogen E-region binding-pocket generated by *ezPocket* tool with the *fconv* method [35,36]. The 3D-lig-plot diagrams for best BTS binding-poses are shown like B) BTS_*pose 1*, C) BTS_*pose 2* and D) BTS_*pose 3* obtained from the docking complexes BTS-fibrinogen, and depicted with their corresponding FEB values in kcal/mol. Herein, gray dotted-lines between the different BTS-poses and the fibrinogen residue interacting atoms represent van der Waals hydrophobic interactions and the blue dotted-lines represent H-bond contacts. The remaining cases like BTS_poses (from 4 to 9) can be found in Fig. SM1 (SI).

respective LPRS-maps, with zero frequency at the center. That is, the line from each pair of points (pixels) was drawn at the center of the 2D-FFT image. This signal spectra representation is simpler to understand, since all its lines are drawn from the same point. Besides the advantage of placing the zero at the center it is the fact that, it fits with continuous frequency spectra signals of the images that are consistent with the modeling principles for complex biological systems, and allow the identification of frequency (spectral) content analysis of a signal just like ligand-protein interaction perturbation-signals. When the input image is continuous, then its signals are aperiodic. This fact places zero frequency at the center of the 2D-FFT frequency spectrum, with the $X[k]$ signals becoming higher in all directions out to infinity [63–65]. As far as our patterns are concerned, the zero frequency components (central peaks) are the largest. This is not surprising because most of the images from nature are in the low frequency range. Also patterns containing vertical (more intense) and horizontal lines (less intense) indicate the existence of components at all frequencies, but their intensity decreases with the frequency. This means that most information is placed in the low frequencies, that is, the more important contributions arise from slow changes in LRSP maps. So, conformational changes spread smoothly along the polypeptide chains. These changes are mostly one-dimensional as the vertical dominant direction suggests. The absence of rotations in the line indicates that none of the BTS-poses involve a rotational movement of the *E*-domain. The most intense 2D-FFT central signals were detected for BTS_*pose 1*, BTS_*pose 2* and BTS_*pose 3* compared to the reference control. For the other BTS-poses, the central peak decreases and higher frequency contributions increase.

3.4. Fractal analysis-based on LPRS-maps of BTS-ligand conformation

Lastly, we examine the theoretical results following a combination of two recognized algorithms for fractal analysis: (i) the Mandelbrot set and (ii) box-counting methods [46,48,51]. The key idea behind such approach is the concept of the fractal protein, through which, the ligand-druggability properties of a simple protein (fibrinogen E-region binding-site) is formally represented as a highly complex fractal form according to non-Euclidean geometry, irregularity properties of the protein surface and the principles of fractal theory [45,47,50].

In this context, the main goal of this approach was to describe the differences in the fractal geometric-pattern of the perturbation responses in the fibrinogen binding-site, derived from the LPRS maps before and after the BTS-docking interactions, from a qualitative and quantitative point of view [63]. From the mathematical point of view, the fractal protein (fibrogen) is a finite square subset of the Mandelbrot fractal set ($\boldsymbol{M}$), with center coordinates (x, y) and sides of length z, defined by a family of complex quadratic polynomials function (f) obtained by using an Iterated Function System (IFS) that is executed in a feedback loop or quadratic recurrence equation given by $\boldsymbol{f_c(z) = z_{n+1} = z^2 + c}$ [46,48,53]. Due to this, it is possible to achieve a high degree of complexity based on the inter-residue network communication derived from its folding properties (roughness), which is more significant in the surfaces of interaction for most of the catalytic binding-sites of the protein (fibrinogen) being able to be disturbed in the presence of certain ligands (BTS).

For this instance, the $\boldsymbol{M}$ set can be defined as the set of all the N-pixels of a given LPRS map image, which represent an unperturbed or perturbed fibrinogen binding-residue in such a way that the previous sequence $\boldsymbol{f_c(z)}$ does not escape to infinity. Then, a complex number $\boldsymbol{c}$ is part of the Mandelbrot set $\boldsymbol{M}$ if, when applying the quadratic recurrence equation, the iterating function $fc(\boldsymbol{z})$ remains bounded. For the first time, the initial value starting with $\boldsymbol{z_n = 0}$ is taken as a critical point like $f_c^n(0)$. Then, we can formally define the Mandelbrot set $\boldsymbol{M}$ as follows:

$$\boldsymbol{M_{set}} = \boldsymbol{f_c^n(z_n)} = \lim_{n\to\infty} \left\| z_{n+1} = z_n^2 + c \right\| \nrightarrow \infty \text{where } z_n = 0 \quad (4)$$

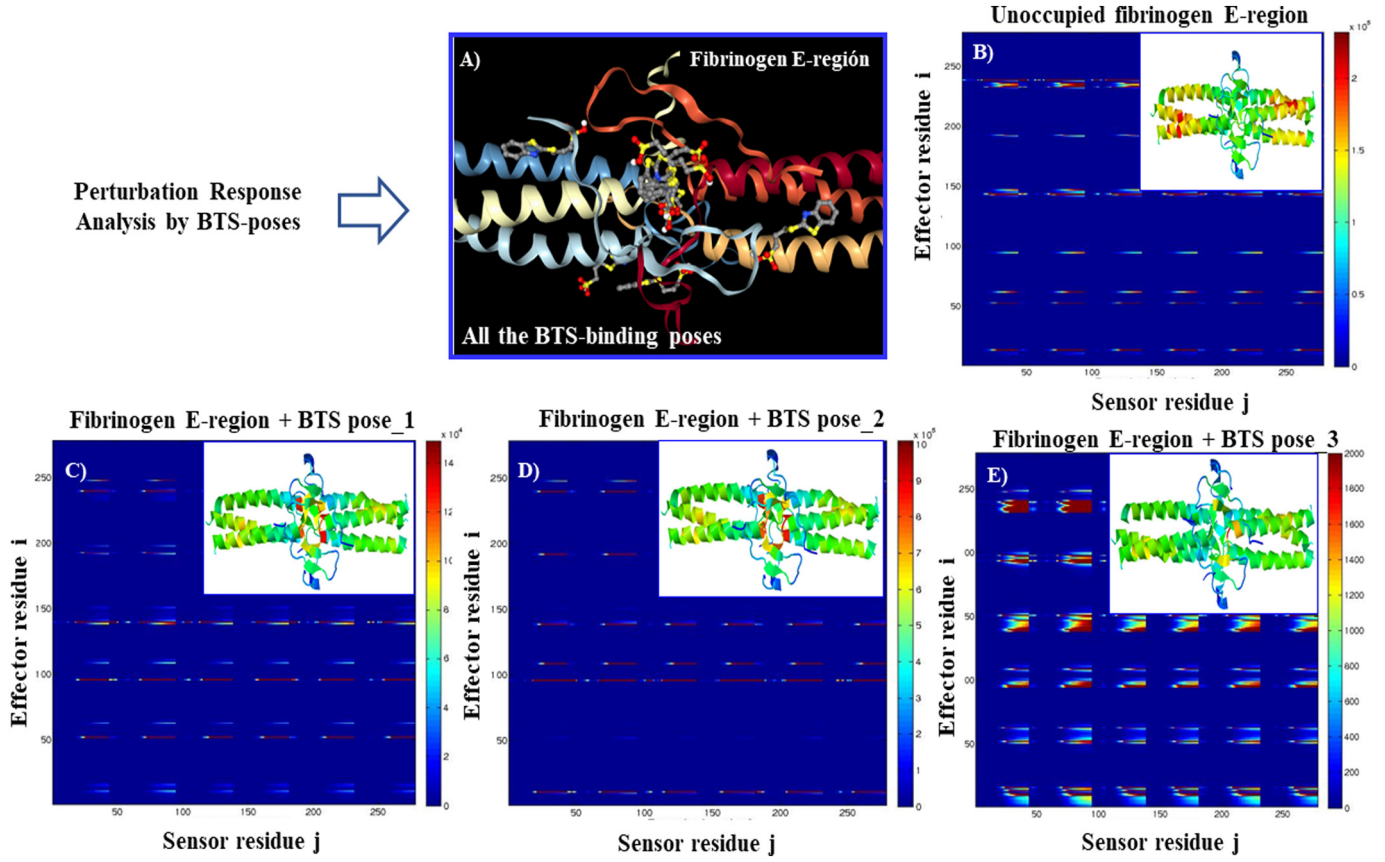

Fig. 2. Perturbation response analysis for the BTS-binding poses. A) 3D-Cartoon representation for all BTS-docking poses superimposed in the fibrinogen E-region binding site, designed using the open-source Pymol visualization system. B) LPRS map obtained for the unoccupied fibrinogen E-region binding site and acting as the control simulation experiment. Individual LPRS-maps obtained from the best BTS-fibrinogen docking complexes-based conformation analysis and the corresponding 3D-fibrinogen E-region structure (for all modes) with intensity bar color (on the right) for: C) BTS_*pose 1*, D) BTS_*pose 2*, and E) BTS_*pose 3*. For this purpose, dark blue to red regions represent the increasing propensity to act as sensor/effector after the stimulus of perturbation (BTS-interaction) for 278 residues analyzed from the fibrinogen E-region like by C(α)-atoms. All the LPRS-maps were established in range of the low frequency normal modes equal to 2. The remaining cases like BTS_poses (from 4 to 9) can be found in the Fig. SM2 (SI).

Here, the IFS output (recursive function) of $f_c^n(z_n)$ is taken as input when the function calls itself and the absolute value of z_n it remains bounded. The vertical brackets denote the Euclidean norm, which is a measurement of how far away a point in the complex plane (k) is from origin: $\|z\| = \sqrt{a^2 + b^2}$. The results obtained by applying the Mandelbrot set approach are presented in Fig. 5.

These Mandelbrot set results refer to the protein-ligand binding condition for the three best BTS-docking *poses_1*–3, in order to identify critical changes in the fractal geometry of the fibrinogen binding residues (*i*-effector and *j*-sensor residues; *RES*) before and after the interaction with the different BTS-binding_*poses* (see Fig. 6).

Let us begin by looking at the fractal patterns in the *n*-cycle components attached within the big region of the Mandelbrot set (*i.e.*, the main *cardioid 1*) and around it. The cardioid image modeling-based Mandelbrot set is defined as the trajectory described by a point (*i.e.* the LPRS map image pixel) of a circle that rolls around another fixed circle with the same radius to get a modified or unmodified cardioid image pixel, which represent differences in the fractal geometry shape of the response (*i.e.* the docking interactions coming from the LPRS maps). That is to say, it represents the trajectory described by any relevant interacting fibrinogen-residues (*RES_fib*) before and after their interactions with the BTS-poses up to 9. For example for the *RES_fib-BTS_pose 1*, these are: PRO49_chain Q, SER50_chain Q, TRH85_chain R, CYS19_chain S, and for the *RES_fib-BTS_pose 2*: TRH21_chain S, TRH22_chain S, SER50_chain Q, CYS83_chain R, SER50_chain N), which together make up the protein binding pocket (please, refer to Fig. 1B and C).

Actually, the main *cardioid 1* comprises a relevant region of geometric parameters for which it has an attracting fixed point with period $n =$ 1. The obtained subsets of the Mandelbrot set (cardioid 1) thus provide relevant information about potential structural changes associated with the fractal geometry of the protein-ligand systems evaluated (unoccupied fibrinogen E-region and BTS-poses at the fibrinogen E-region). Indeed, previous works have suggested that changes in the spatial ordering of protein binding residues induced by certain stimuli (like ligands) can modulate the binding properties of the protein through changes in its fractal dimension (FD) [66,67]. It is well known that the FD is associated to the backbone non-Euclidean geometry, as well as to the irregular nature and fractal surface properties of the binding sites. This is justified by the fact that most of the ligand-protein interaction processes occur under strict conditions of ligand-specificity and, at the same time, that these processes depend on surface phenomena with a defined geometric pattern of complementarity [68,69]. We thus suggest that small changes in the fractal surface patterns, such as the cardioid 1 subset, could affect not only the native fibrinogen folding and solvent accessible surface in the unbound state (unoccupied fibrinogen E-region), but also the conformational entropy and thermodynamic stability of the docking complexes formed between the fibrinogen E-region and the different ligands [66,67]. The major contribution to these changes comes from the establishment of van der Waals and H-bond interactions mainly with fibrinogen *i*-effector residues from the chains N, Q, R, and S. It is therefore easy to identify dissimilarities between the fractal patterns-based subsets of the Mandelbrot set for the best BTS conformations evaluated (BTS-binding poses_1–3), which are mainly concentrated in the ***M*** region (*cardioid 1*) in its positive (*ImX*[k]) and negative (*ReX*[k]) quadrant, predicting changes in the geometric complementarity of the *i*-effector residues from chains N, Q, R, and S. In

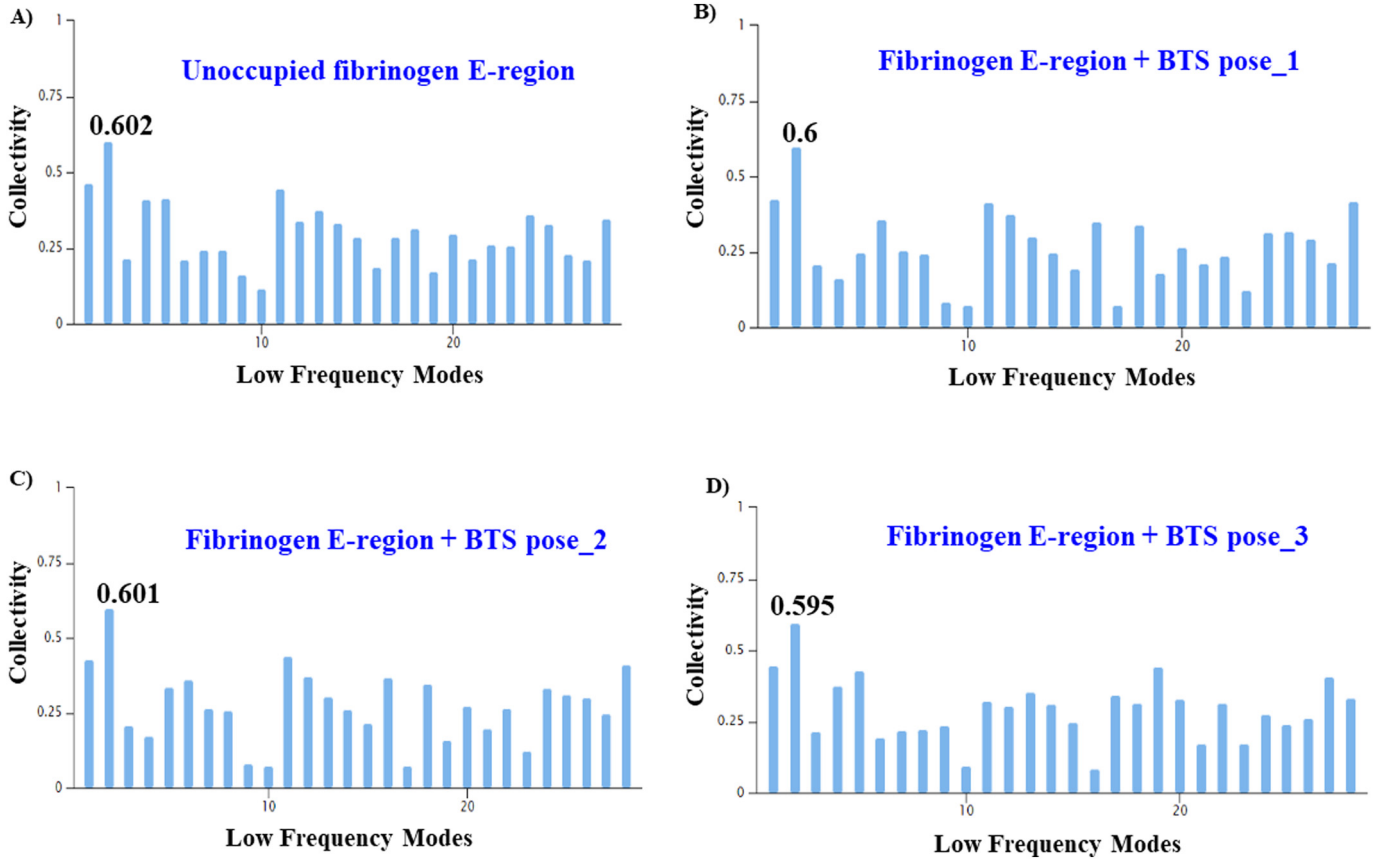

Fig. 3. Graphical representation of the degree of collectivity $K(k)$ *vs.* low frequency normal modes (mode 2) for the control A) unoccupied fibrinogen E-region (0.602), and for the three best BTS-binding poses, namely: B) Fibrinogen + BTS_*pose 1* (0.6), C) Fibrinogen + BTS_*pose 2* (0.61), and D) Fibrinogen + BTS_*pose 3* (0.59). The remaining cases can be visualized in Fig. SM3 (SI).

addition, the changes can be confronted with those from the Mandelbrot set of the control (unoccupied fibrinogen E-region) in the same quadrant. By the other hand, the differences observed between the best BTS-binding poses_(*1–3*) evaluated and the unoccupied fibrinogen E-region in the small quasi circular-shaped region, named *cardioid 2*, which is located in the left-site of *cardioid 1* with negative real and imaginary components, -*ReX*[*k*] and -*ImX*[*k*], respectively. The fractal-geometric differences in *cardioid 2* are maybe associated with changes in the geometric parameters for the clusters of *j*-sensor residues (allosteric residues), for which the attracting cycle has a period of 2 following complex geometrical criteria. Furthermore, other different fractal-patterns were detected for an infinitely many other periodic components like small *cardioids* tangent to *cardioid 1* and *cardioid 2*, such as ***M***-submaps of *n*-cycles (called *hyperbolic components*) that exhibit a "*chaotic*" behavior, plotted in the interior regions of ***M*** and over *Julia sets J*(*f*) [49].

In order to quantify potential fractal geometrical perturbations between the formed docking BTS complexes and the fibrinogen binding-site, we calculated their fractal dimensions by using the box-counting algorithm [51]. Notice that one of the most important properties in the fractal analysis is the degree of self-similarity. For instance, a topological fractal dimension near to 2 is considered to embody high complexity (high variety of geometrical information) and low self-similarity, while a topological fractal dimension closer to 1 represents little complexity and high self-similarity [47]. Following these criteria, the LPRS-maps were analyzed using the box counting algorithm and the obtained results are shown in Fig. 7. For this instance, the non-Euclidean geometrical patterns were characterized according to the fractal dimension like D_{BW}, which describes the LPRS maps properties by considering the border of LPRS map fractal pattern. $D_{BBW,}$ characterizes the LPRS map-fractal pattern on the white background, and the D_{WBW} the LPRS map-fractal pattern on the black background of the images calculated for each BTS-*poses_1–9*.

The calculated FDs are associated to the fibrinogen surface and backbone non-Euclidean geometry. These can show how the protein folding, packing density, solvent-accessibility, crystallographic positioning and binding-interaction properties can be affected under the influence of different conformation of the BTS-ligand in the fibrinogen binding-site. Especially, by the number of van der Waals docking-interactions through the different BTS-binding modes, degree of collectivity $K(k)$, and van der Waals distances of interaction (≤7 Å). Herein we suggest that, BTS-ligand binding modes lead to a change in roughness-based FDs [64]. Because we detect that the fractal dimensions (D_{BW} ~ 1.05 and D_{W+BW} ~ 1.07) were higher for all the BTS-*poses_1–9* complexes at the fibrinogen E-region compared to the physiological condition of unoccupied fibrinogen E-region binding site used as control (D_{BW} = 0.94 and D_{W+BW} = 0.96, respectively). As mentioned above, a FD (D_{W+BW}) ≈ 2 reveals high variety of geometrical information and low self-similarity, while FD (D_{W+BW}) ≈ 1 represents little complexity and high self-similarity. It is important to note here that, the fibrinogen protein is a large macromolecule and its vibrations generate a huge amount of different conformational sub-states (normal modes-based degree of collectivity) under BTS-ligand interaction, which can be associated with local perturbations (*i.e.*, variation in the local magnitudes of calculated FD from the fibrinogen + BTS complexes).

By the other hand, the value of the D_{B+BW} remained fixed around 1.99 in all the cases, thus revealing high complexity of geometrical information. The latter suggest that the BTS-ligand can induce significant changes in the geometrical selectivity-based FD of the fibrinogen E-region binding site. It is well-known that changes (*global* and *local perturbations-induced by ligands*) in the spatial arrangement of atoms in key residues (like perturbations-induced on *j*-allosteric residues) of

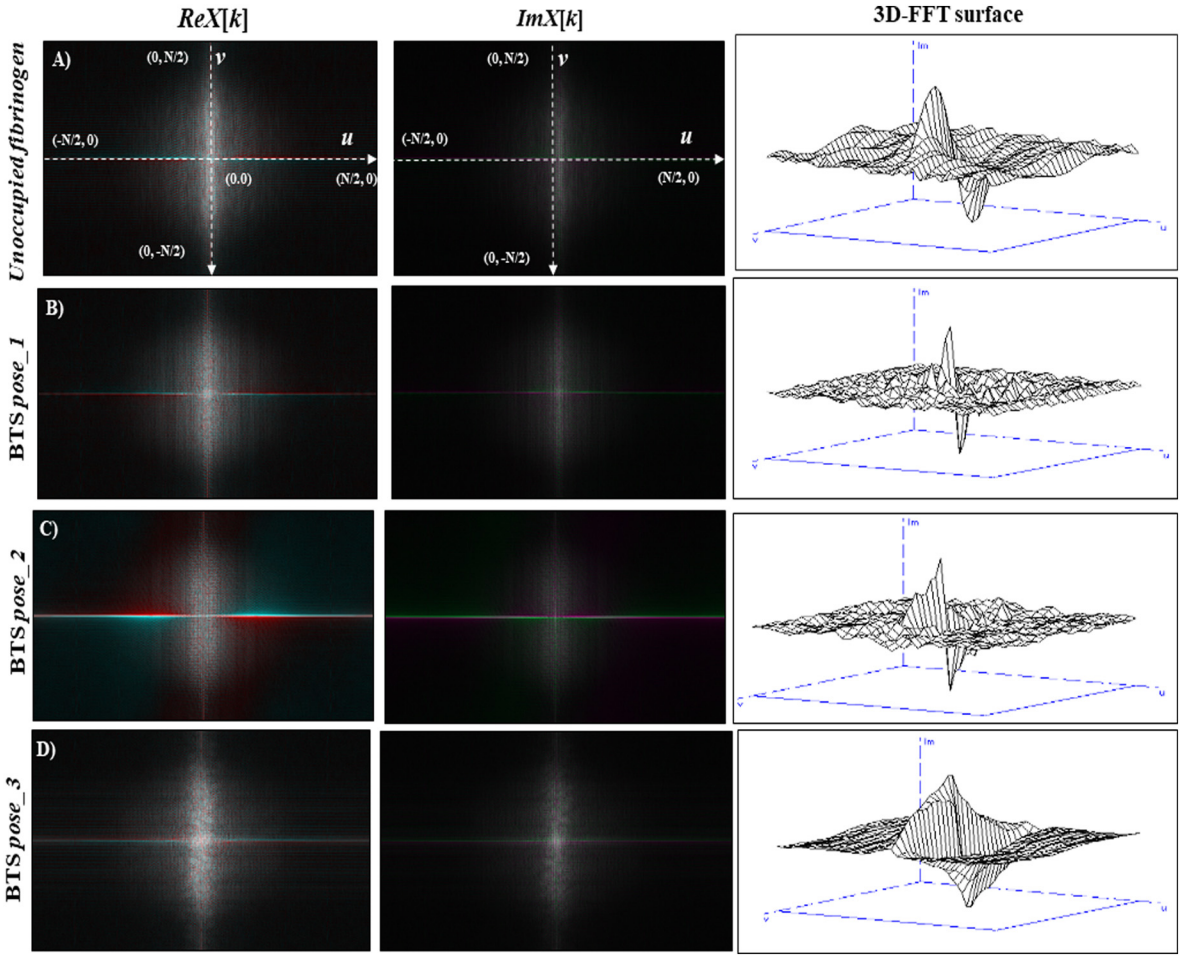

Fig. 4. Graphical representation of the 2D-FFT profiles of the frequency domain ($X[k]$) based on the real component ($ReX[k]$) and its imaginary component ($ImX[k]$), as well as the 3D-FFT surface graph with $ImX[k] \neq 0$ and $ReX[k] = 0$ obtained from the LPRS-maps for the control A) unoccupied fibrinogen, and for the three best BTS-crystallographic conformational binding modes, *i.e.*: B) fibrinogen plus the BTS_*pose 1*, C) fibrinogen plus the BTS_*pose 2*, and D) fibrinogen plus the BTS_*pose 3*. For all the 3D-FFT surface graphs, the coordinates axes (u, v) are included into the spatial frequency to obtain the corresponding signal 3D-frequency domain ($X[k]$) based on the imaginary dimension, the latter representing the signal perturbation-response (BTS pharmacodynamic interactions) depicted in the complex plane k from a qualitative point of view. The remaining cases can be visualized in Fig. SM4 (SI).

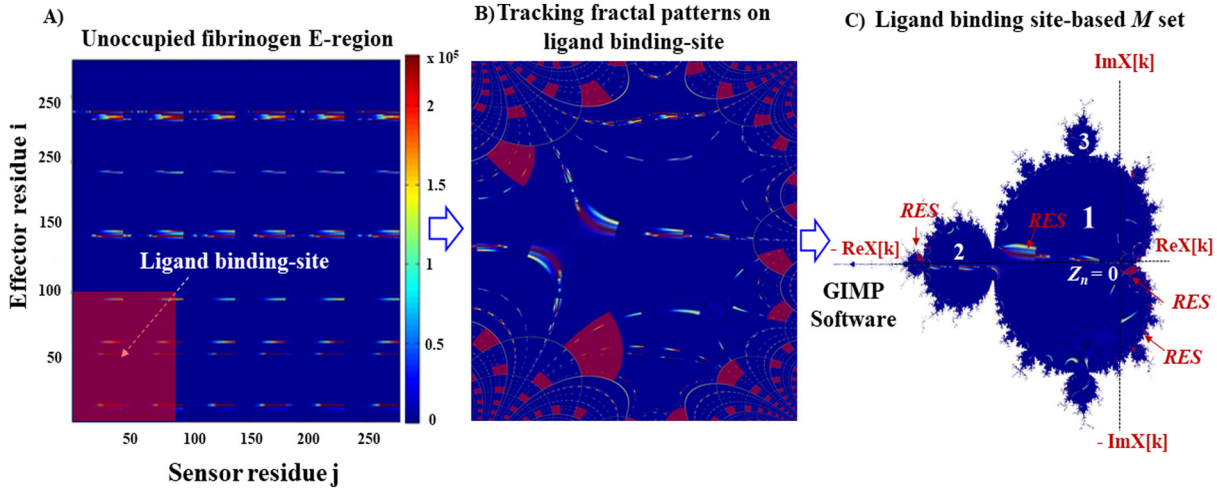

Fig. 5. A) LPRS map for unoccupied fibrinogen (control) highlighting the fibrinogen binding-site (*i.e.*, the interacting residues from E-region are included in the transparent red rectangle). B) Data visualization-based tracking fractal patterns of the fibrinogen binding-site. C) Data visualization-based Mandelbrot set fractal approach with cardioid image modeling obtained for unoccupied fibrinogen binding-site with different positions for the ligand binding-site residue cluster (*RES*) in the relevant Mandelbrot cardioid (*i.e.*, cardioids 1, 2) considered like unperturbed fibrinogen residues (*RES-unbound*). The Mandelbrot set parameters are fixed at $ReX[k]_{max} = +1$, $ReX[k]_{min} = -2$, $ImX[k]_{max} = +1$, and $ImX[k]_{min} = -1$ for comparison purposes with the different BTS-poses.

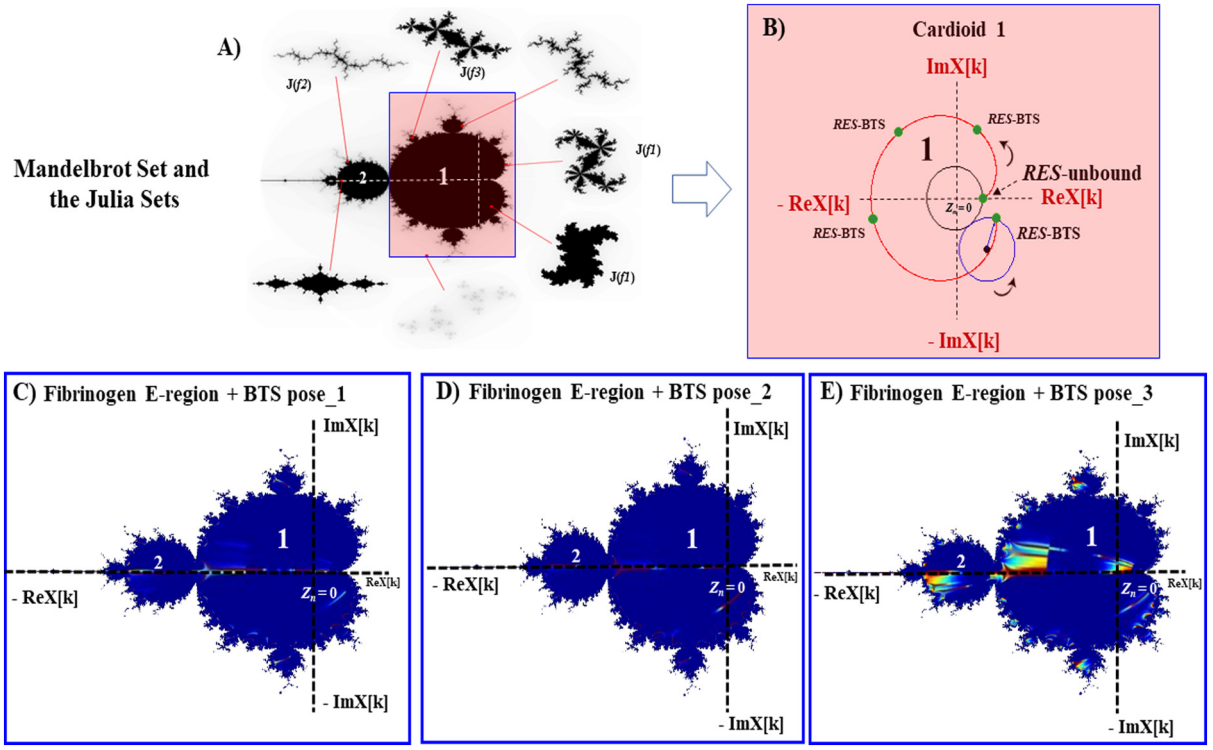

Fig. 6. Data visualization subsets of the Mandelbrot set fractal approach with cardioid image modeling from LPRS maps. A) Canonical representation of the *M* set with the main cardioids (1 and 2) and the corresponding Julia sets ($J(f2)$, $J(f3)$ and $J(f4)$). B) Geometrical representation of the different positions of a given fibrinogen residue cluster (*RES*; green dot) in the main Mandelbrot cardioid (*i.e.*, cardioid 1) considered like an unperturbed fibrinogen binding-site residue cluster (*RES-unbound*) in $z_n = 0$ before BTS-interaction, and the same perturbed fibrinogen residue cluster (*RES-BTS*) after BTS-interaction in the complex plane *k*. In addition, the data visualization subsets of the Mandelbrot set fractal approach for the three best BTS-ligand binding modes are shown. C) Fibrinogen + BTS_*pose 1*, D) Fibrinogen + BTS_*pose 2*, E) Fibrinogen + BTS_*pose 3*. The Mandelbrot set parameters are fixed at $ReX\ [k]_{max} = +1$, $ReX\ [k]_{min} = -2$, $ImX\ [k]_{max} = +1$, and $ImX\ [k]_{min} = -1$. The remaining cases can be found in Fig. SM6 (SI).

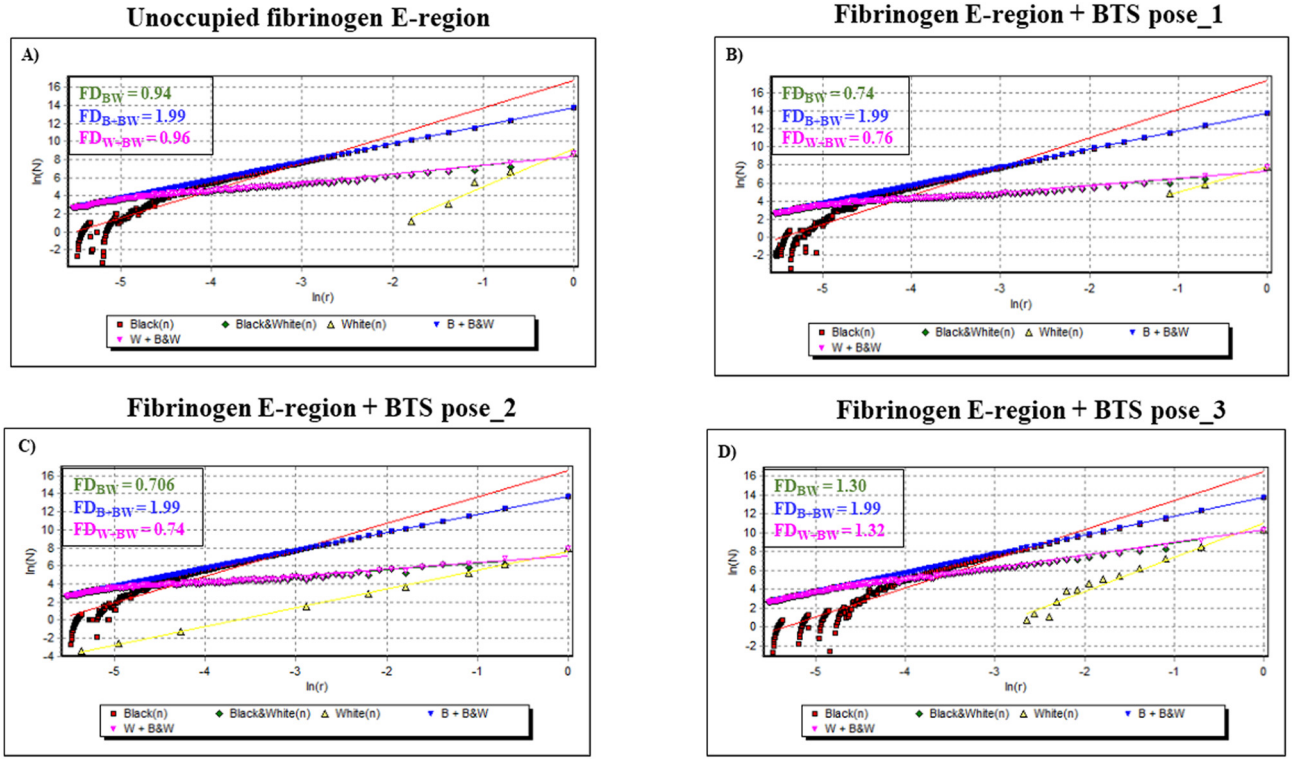

Fig. 7. Fractal spectrum based on the box-counting algorithm applied to obtain the slopes of the linear regression yields from binary black/white LPRS maps image-processing. These slopes correspond to the fractal dimensions (*FD*: D_{BW}, D_{BBW}, and D_{WBW}) for the A) unoccupied fibrinogen binding-site and the best docking complexes like: B) fibrinogen + BTS_*pose 1*, C) fibrinogen + BTS_*pose 2*, and D) fibrinogen + BTS_*pose 2*. The remaining cases can be seen in Fig. SM7 (SI).

proteins can be described by their fractal dimension. Besides these changes can negatively impact the biological function of proteins, particularly when they affect the structural properties of the binding cavities, which are essential in the complementary processes of ligand geometrical specificity and recognition [63]. However, we note that the values of the D_{BW} and D_{W+BW} are very close to each other for the different BTS-poses complexes at the fibrinogen E-region. This in turn might be related with the very close strength of the Gibbs free binding energies (FEB values) obtained for most of the evaluated cases. The highest values for FD were found for the system BTS *pose_3* at the fibrinogen E-region ($D_{BW} = 1.30$ and $D_{W+BW} = 1.32$), which presents an average FEB = −5 kcal/mol. In this case, we suggest that the fractal structure of the local perturbation response maps obtained for the BTS *poses_1–9* exhibit low variety of geometrical information and high statistical self-similarity among them. In this regard, a fractal is considered as rigorously self-similar, if it can be expressed as a union of sets, each of which is an exactly reduced copy of the full set of points, taken as perturbed and unperturbed fibrinogen binding site residues (E-region). Additional details on black/white binary LPRS map image-processing can be found in Fig. SM8.

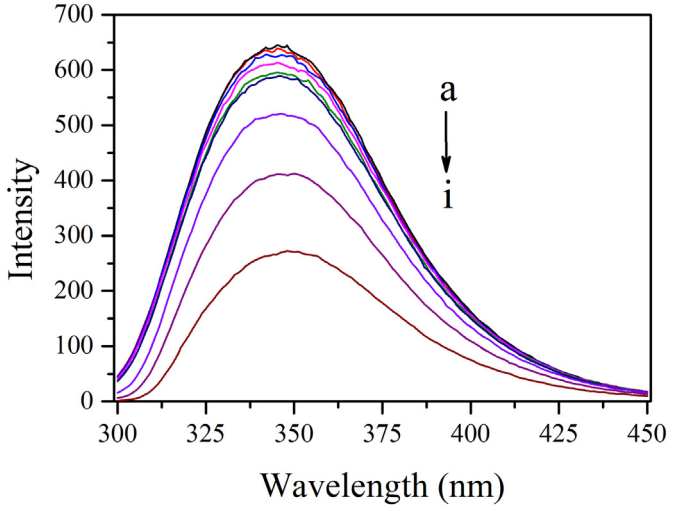

Fig. 9. Fluorescence emission spectra of Fibrinogen in the absence and presence of different concentrations of the BTS drug. Fibrinogen concentration: (a-i) = 1 μM. BTS concentrations: (a-i) = (0, 1, 2, 4, 8, 10, 50, 100, 200 μM).

3.5. Experimental characterization

To further complete our computational results, we have performed several experiments. First, we have explored the energetics of BTS fibrinogen interactions by means of ITC. Characteristic microcalorimetric titration profile for the binding of BTS with fibrinogen is shown in the left side of Fig. 8. Each point corresponds to the heat involved in a single injection of BTS (0.033 mM) into the fibrinogen solution (1 mM), corrected by subtracting the heats of mixing and dilutions. As represented in Fig. 9 the aspect exposes an exothermic process with saturation occurring at BTS/fibrinogen molar ratio higher than 1. With regard to the kinetic evolution of the fibrinogen/BTS complex, the equilibrium is reached after 150 min (obtained from calorimetric raw data). Experimental points were fitted according to the independent binding model in order to obtain the relevant thermodynamic parameters of the binding process. Other binding models were also checked but large uncertainties were obtained for the associated binding parameters. Thus, the obtained values were: 0.98, 6.27×10^4 M^{-1}, −7.30 kcal/mol and − 2.55 cal/mol^{-1} $°C^{-1}$ for stoichiometry, binding constant, enthalpy and entropy, respectively. The stoichiometry reveals that only one type of binding takes place. The binding constant suggests that BTS is a moderate binder. The obtained enthalpy and entropy values are negatives. Referring to enthalpy, this means that the binding is driven by the formation of non-covalent bonds (hydrogen bond, electrostatics, π-π interactions); in the case of negative entropy change, it reveals hydration and a loss of conformational freedom associated with the complex formation [70]. In a previous study we analyzed the self-aggregation process of BTS in aqueous solution by molecular dynamics, observing that the number of water molecules around BTS decreases slightly when a transition from monomeric to aggregated state occurs [16]. Bearing in mind the similarities between binding and micellization process, we can conclude that desolvation is not present in this binding process as entropy has already been pointed out. In connection with the free binding energy, the value obtained from ITC is −6.54 kcal/mol, which is in really good agreement with that predicted by docking analysis, notably for BTS pose_1 and BTS pose_2, both in the quantities (−7 and −6.8 kcal/mol, respectively) and in the presence of hydrogen bonds and van de Waals hydrophobic interactions. Amaral et al. [71] highlighted the differences in the thermodynamic quantities when the ligand binds to a loop (loop-in compound) or an helix (helix-binding compound). Basically, loop-in binding compounds are primarily enthalpically driven, with favorable or small entropic contributions. In contrast, for the helix-binding compounds, there is a large favorable entropic contribution to binding, and most of them have a binding enthalpy penalty. Clearly, our results evidence that BTS is a loop-in compound. This is another interesting point because docking

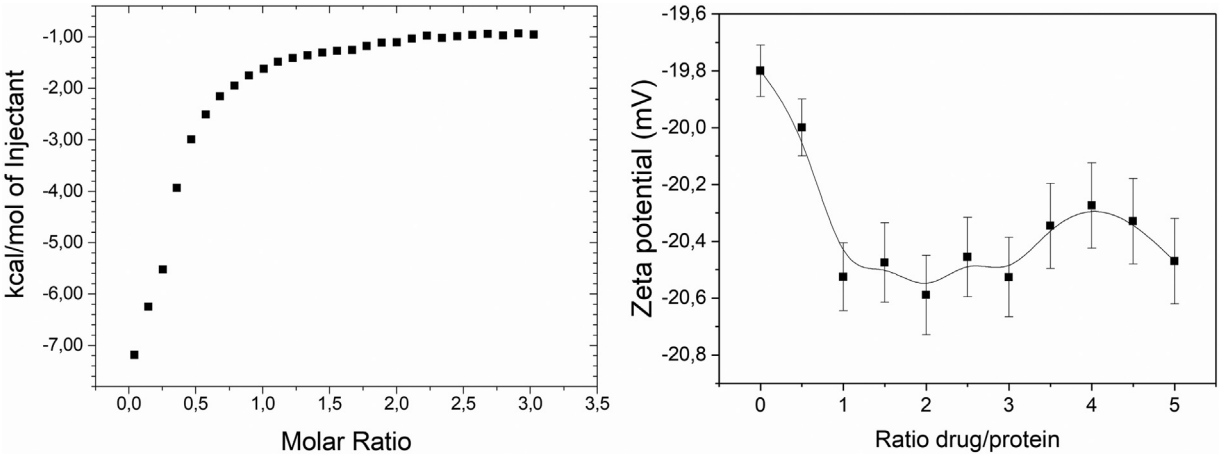

Fig. 8. (Left) Enthalpy as a function of molar ratio (BTS/fibrinogen). Experiments were performed by adding 1 mM BTS solutions into 0.033 mM of fibrinogen. (Right) Zeta potential of the complex BTS-fibrinogen as a function of drug-fibrinogen molar ratio.

results for BTS pose_1 and pose_2 reveal interactions with residues places between the 5-turn (or 5-turnI) and NCap (see Fig. 1). On the other hand, entropy change upon binding may arise from a reduction in translational and rotational degrees of freedom, an alteration of the conformational flexibility of the binding partners, and from the reorganization of their solvation shells upon binding. Having ruled out desolvation effects, we then focus on conformational changes. In our perturbation analysis we have calculated the vibrational modes and protein flexibility pre and following BTS binding. The obtained degree of collectivity of fibrinogen was 0.602 (mode 2), while for the BTS pose_1 and BTS pose_2 decrease slightly to 0.6 and 0.601, respectively. This subtle decrease also manifests itself in all the other analyzed modes. A high degree of collectivity means a highly cooperative mode that enrolls a portion of the protein. Thus, upon binding cooperativity decrease, and also conformational flexibility, become the main contribution to entropy change.

Fig. 8 shows the zeta potential values of the systems under study as a function of the drug-protein molar ratio. At low drug concentrations (lower ratio) zeta potential increases fast, then becomes practically constant (plateau) for drug:protein molar ratio over 1.0. At this pH (8.5) the net charge of the fibrinogen is negative, thus the cationic moiety of the drugs interacts mainly electrostatically with the opposite charged residues of the protein. This results in a specific and non-cooperative binding. It is clear that the electrokinetic characterization of the complexes follows quite well the same pattern as those found from ITC measurements.

Fig. 9 shows the influence of BTS on fluorescence emission spectra of fibrinogen. The fluorescence emission peak of the fibrinogen alone can be found at about 350 nm at the excitation wavelength of 280 nm. As the concentration of the drug was increased, the peaks suffered a gradual red shift to 353 nm. Simultaneously, the fluorescence emission intensity decreased regularly. From previous works, it is known that those changes in fluorescence are correlated with the number of cleaved disulfide bonds upon irradiation and the reduction of the disulfide bond makes the fluorescence intensity higher [72]. In this context, one may suggests that the interaction of the BTS with fibrinogen causes the raise in the polarity of its aromatic residues mellieu, being more hydrophilic with the increase of the drug in the solution which resulted in the decrease and red shift of the fluorescence [73]. Since the interaction has to occur in the pocket at *E*-domain, we identified two residues, [Tyr]18:S and [Tyr]18:P, as the main responsible for this shift due to changes in their environment.

Considering that the binding sites were independent and non-interactive, the Stern-Volmer equation was used to study and analyze further the intrinsic quenching fluorescence [74].

$$\frac{F_0}{F} = 1 + K_{sv}[BTS] \tag{5}$$

F_0 and F are the fluorescence emission intensities with the presence or absence of BTS; [BTS] is the drug concentration and K_{sv} the Stern-Volmer quenching constant.

According to the Stem Volmer equation, the linearity of F_0/F *versus* the drug concentration, [BTS], reveals the quenching type. In this system, linear correlations were probed at different temperatures with different values of R coefficient, meaning that all Trp(s) present in the macromolecule differ slightly in accessibility [75]. The slope of the straight line gives the K_{sv} value of $(6.56 \pm 0.3) \times 10^3$ L mol^{-1} at 298.15 K. Since the fluorescence lifetime of the fibrinogen in water is 10^{-8} s^{-1}, and considering that: $K_q = K_{sv}/\tau_0$, the K_q can be obtained and has a value of 6.56×10^{11} L M^{-1} s^{-1}. The maximal dynamic quenching constant of the studied biopolymer is 2.0×10^{10} L M^{-1} s^{-1} [76]. So, in this case, is safe to assure that the quenching of fibrinogen by BTS is not initiated by dynamic collision but from the formation of a complex [77].

Fluorescent measurements are also a great tool to get quantitative information about the static quenching process [78]. The binding constant (K_a) and the number of binding sites (n) can be obtained using the following equation:

$$log\frac{(F_0 - F)}{F} = logK_a + n \cdot log[BTS] \tag{6}$$

Accordingly, the slope of the linear plot of log $[(F_0 - F)/F]$ as a function of $log[BTS]$ gives the stoichiometry of binding [79], while the binding constant can be obtained from the intercept. In the present case, the values of n and K_a are 0.86 ± 0.05 and $(1.76 \pm 0.25) \times 10^3$ M^{-1}, respectively. That means that fibrinogen interacted with BTS in one independent class of binding sites, forming a 1:1 complex.

As shown in Fig. 10, the great overlap between the absorbance spectrum of the complex and the normalized fluorescence spectrum, it can be presumed that the molecular details of the complex formed between the fibrinogen and the drug are obtained from non radiation energy transfer, as the fluorescence spectroscopy of the donor is not malformed. According to Förster theory of non-radiation energy transfer

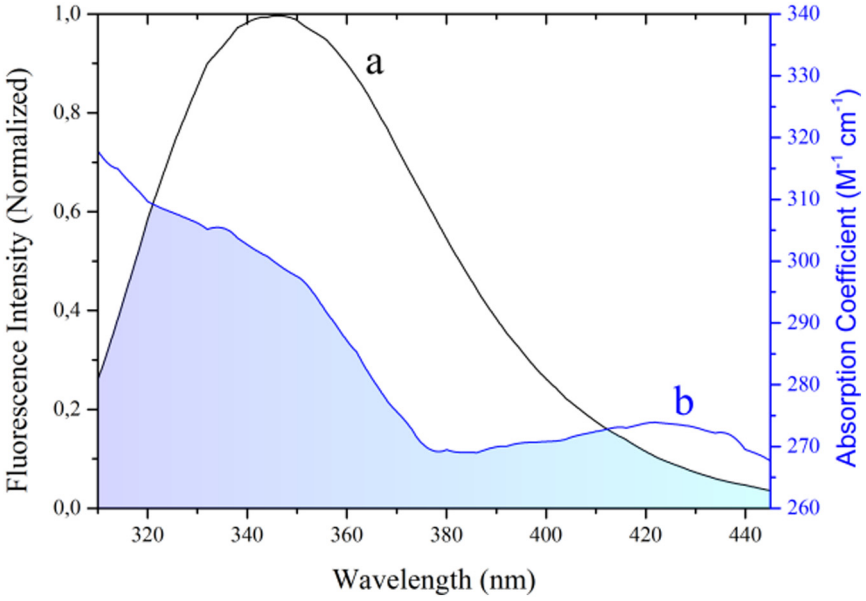

Fig. 10. Overlap of the normalized fluorescence spectrum of fibrinogen and the absorbance spectrum of the complex. [Fib]/[BTS] = 1.

[80], the average spatial distance between the probed and excited transition dipoles can be estimated using the Förster-energy transfer rate equations [81]:

$$k_T(r) = \frac{Q_D \kappa^2}{\tau_D r^6}\left(\frac{9000\,(\ln 10)}{128\,\pi^5 N n^4}\right)\int_0^\infty F_D(\lambda)\varepsilon_A(\lambda)\lambda^4 d\lambda \quad (7)$$

$$J(\lambda) = \frac{\int_0^\infty F_D(\lambda)\varepsilon_A(\lambda)\lambda^4 d\lambda}{\int_0^\infty F_D(\lambda)d\lambda} \quad (8)$$

$k_T(r)$ is the transfer rate for a donor and acceptor separated by a given distance, r [82]. Q_D is the quantum yield of the donor in the absence of acceptor; κ^2 is a factor that describes spatial orientation factor of the dipole, ($J(\lambda)$) expresses the overlap integral between the fluorescence emission spectra of donor and the UV absorption spectra, $F(\lambda)$ is the fluorescence intensity of fluorescence donor when the wavelength is λ, $\varepsilon(\lambda)$ is the molar absorption coefficient of the acceptor at the wavelength of λ. (E) is the efficiency of energy transfer and is related to the fraction of photons absorbed by the donor and transmitted to the acceptor. Commonly, efficiency is obtained from the relative fluorescent intensity of the donor in the absence (F_D) and presence (F_{DA}) of the acceptor through the following equation:

$$E = 1 - \frac{F_{DA}}{F_D} = \frac{R_0^6}{R_0^6 + r^6} \quad (9)$$

where R_0 is the critical distance when the transfer efficiency equals to 50% ($R_0^6 = 8.79\,x\,10^{-5}(\kappa^2 n^{-4} Q_D J(\lambda))$). In the present work, n is given by the refractive index of water, 1.333, κ^2 is 2/3, and the Q_D is 0.15, coinciding with the fluorescence quantum yield of tryptophan. Combining the above equations, the following values were determined: $J = 4.79 \times 10^{12}\ M^{-1}\ cm^{-1}\ nm^4$, $E = 0.08$, $R_0 = 1.54$ nm, and $r = 2.29$ nm. As the distance between the donor and the acceptor is within 2–8 nm it is safe to assure that the energy transfer between fibrinogen and BTS is very probable and it demonstrates the presence of non-radiation energy, meaning that the most excited elements could decay to the ground state. [83,84]. Once again, these results reinforce the hypotheses formulated in the computational section.

In order to evaluate the impact of BTS in the fibrinogen conformation, the scattering of BTS-containing solution was first investigated at 70, 110, 150 and 180 mM. Fig. 11 presents the pair distribution functions, p(r), calculated for each experimental curve displayed in the inset.

As one can observe, the p(r) functions exhibit an oscillatory profile, typical of core-shell like aggregates with two regions of distinct electron densities in respect to that of the solution [30]. Such aggregates have maximum dimension around 50 Å. Of note, the core-shell like structure is not well formed at 70 mM BTS according to p(r) function, unlike the results obtained from BTS at concentrations greater than 110 mM. Therefore, we may infer that BTS molecules form pre-aggregates at the lowest investigated concentration, evolving to core-shell like aggregates with drug concentration increase.

As previously suggested by NMR analysis of BTS aggregates between 50 mM and 290 mM, the shape and size of the small self-organized BTS are very similar independently of the concentration [26] as observed here. Further, it was possible to suggest the presence of small BTS aggregates even at low concentrations (below cmc ~ 170 mM).

Taken into account the SAXS curve for the drug-free fibrinogen solution at 0.5 mg/mL (data not shown) we obtained the same result as already reported by our group [29]: the protein coexists as 63% of the paired-dimers and 37% of the dimers.

Subsequently the evaluation of the BTS and fibrinogen pure solutions, now we present the SAXS data obtained from fibrinogen mixed to BTS solutions at different concentrations. Fig. 12 shows the SAXS results.

For the fibrinogen in the presence of 70 mM BTS, the experimental SAXS curve (black circle) is consistent with the sum of the scattering of the protein and 70 mM BTS for q values higher than 0.07 A^{-1}. A similar trend happens for the SAXS curves of fibrinogen in the presence of 110 (blue), 150 (green) and 180 (red) mM, in which the experimental curves are compatible with the sum of independent scatterings (triangles) for each case for $q > 0.04\ A^{-1}$. Such q range is related to the BTS self-assembled (Fig. 11). We can thus suggest the presence of BTS aggregates in the sample containing fibrinogen too. On the other hand, at low q range (related to the protein tertiary and quaternary structure), the experimental curves are different from the ones obtained by the sum (open triangles) of protein and BTS in solution for all drug concentration. In particular, the experimental scattering intensities are higher than the hypothetical sum of individual scatterings. Such finding suggests the formation of fibrinogen oligomers complexed to BTS since I (0) is proportional to the molecular mass of the scattering complexes [85]. Of note, it was not possible to evaluate the complex molecular mass from I(0) value. This because I(0) usually is determined as an extrapolation of Guinier's law for q - > 0 [86]. However, the Guinier's q region restricted to q_{max} x Rg < 1.3 (where Rg = radius of gyration) was not obeyed in these experiments (Fig. 12).

It is also important to remark that a transition in the fibrinogen aggregation process must take place between 70 mM BTS and 110 mM BTS, due to the quite different scattering profiles at low q range exhibited from these two experiments. However, with the increase of drug concentration the SAXS curves are similar for $q < 0.03\ Å^{-1}$. This gives us an insight that similar protein–BTS complexes coexist with BTS aggregates in 110 mM to 180 mM BTS-containing solution.

4. Conclusions

In the present study, we evaluated the influence of different BTS-ligand conformation binding modes under the interaction with protein fibrinogen by using molecular docking simulations. The computational results showed that the Gibbs free energy of binding values for the obtained docking complexes (BTS *poses*_1–9 at the fibrinogen E-region) were very close in most of the cases, and indicating also that their formation is related to spontaneous thermodynamic processes. We suggest that the differences detected in the FEB values for the nine BTS-poses may be explained based on the different composition and binding properties of the interacting residues present in the biophysical environment of the fibrinogen binding-site (E-region). Besides, the mechanism of docking for the different BTS-binding poses appears to be mainly due to non-covalent hydrophobic interactions, like Π-Π stacking ones, and associated to H-bonding, which together contributes to the stability of the formed complexes. The experimental results from ITC confirmed the results from Gibbs free energy of binding and the interactions involved in the process. In addition, we suggest that the different BTS-binding poses can induce simultaneous modulation (changes) of several target residues (*i.e.* of effector and allosteric residues), based on the results of the local perturbation-response scanning maps, by affecting the inter-residue communication and flexibility-properties of the fibrinogen E-region residue network, according to the most negative FEB values of interaction (BTS-binding poses 1 to 3) obtained. Likewise, we show that all the BTS-binding poses can directly affect the normal modes of flexibility by decreasing the collectivity degree in the fibrinogen binding-site (residues of E-region). The UV–vis and fluorescence measurements supported the latter results. Regarding the LPRS maps image-processing combining 2D-fast Fourier transform and fractal approaches, it revealed significant differences in the frequency domain signals of the BTS-interaction attributed to small conformational changes through the fibrinogen chain. These results were confirmed by SAXS measurements that not only corroborated the presence of conformational changes in fibrinogen protein,

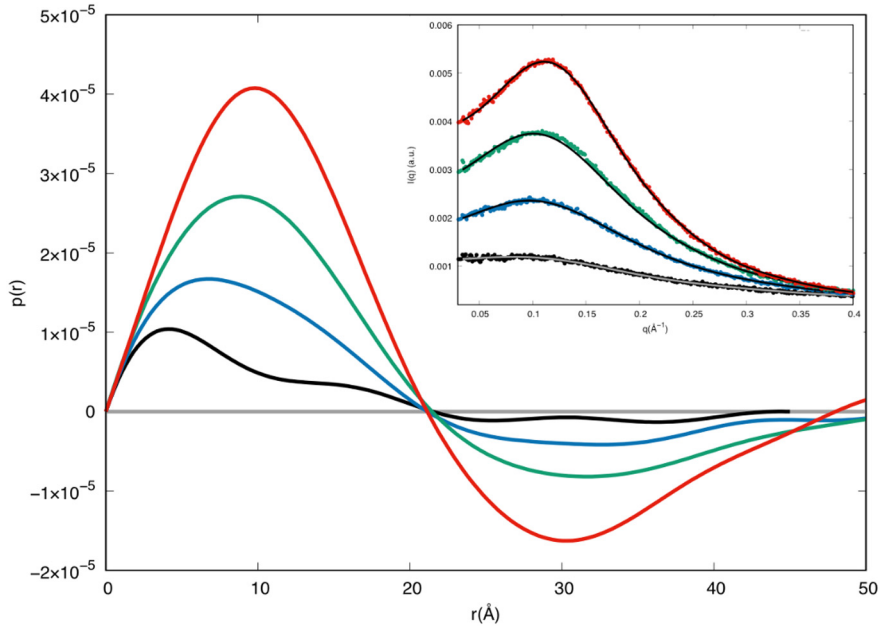

Fig. 11. Pair distribution function calculated for the experimental SAXS curves for 70 (black), 110 (blue), 150 (green) and 180 mM (red) of BTS solution in the absence of fibrinogen. The experimental SAXS curves along with the corresponding I(q) from p(r) (solid lines) are presented in the inset. The p(r) functions were calculated by using GNOM software [31].

but were also dependent on drug concentration. These results open new horizons on understanding the influence of conformational binding modes in protein-ligand interactions, which is of paramount importance in rational drugs-design.

Acknowledgements

The authors acknowledge Ministerio de Ciencia e Innovación (PID2019-111327GB-100) and Xunta de Galicia (ED41E2018/08), G. Scanavachi thanks to CAPES PhD fellowship. R. Itri is recipient from National Council for Scientific and Technological Development (CNPq, Brazil) research fellowship. The work of M. G.-Durruthy and M. N. D. S. Cordeiro was supported by UIDB/50006/2020 with funding from FCT/MCTES through national funds. The authors would also like to thank to the LNLS/CNPEM (Campinas, Brazil) for the use of SAXS beamline.

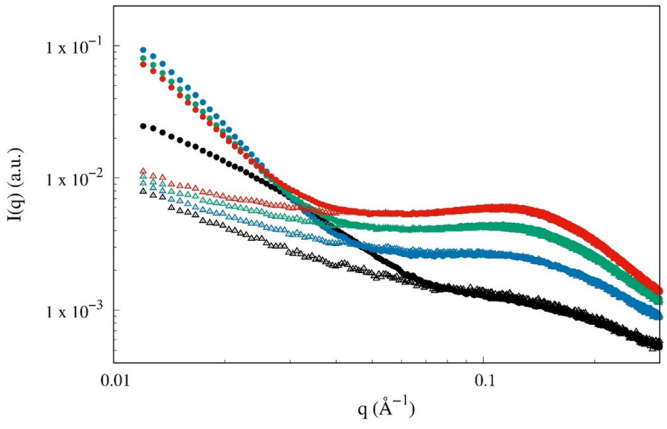

Fig. 12. Experimental SAXS curves (solid symbols) for the fibrinogen (0.5 mg/mL) in the presence of 70 (black), 110 (blue), 150 (green) and 180 mM (red) of BTS. Expected SAXS curves (open triangles) by considering two independent scatters in solution: 0.5 mg/mL fibrinogen and BTS at 70 (black), 110 (blue), 150 (green) and 180 mM (red).

Appendix A. Supplementary data

Supplementary data to this article can be found online at https://doi.org/10.1016/j.ijbiomac.2020.07.044.

References

[1] T. Ando, J. Skolnick, Crowding and hydrodynamic interactions likely dominate in vivo macromolecular motion, Proc. Natl. Acad. Sci. 107 (2010) 18457–18462.
[2] J.M. Ruso, N. Hassan, Role of biomacromolecules in biomedical engineering, Curr. Top. Med. Chem. 18 (2018) 1171–1187.
[3] A. Lopes, S. Sacquin-Mora, V. Dimitrova, E. Laine, Y. Ponty, A. Carbone, Protein-protein interactions in a crowded environment: an analysis via cross-docking simulations and evolutionary information, PLoS Comput. Biol. 9 (2013), e1003369. .
[4] S. Akira, S. Uematsu, O. Takeuchi, Pathogen recognition and innate immunity, Cell 124 (2006) 783–801.
[5] E.A. Meyer, R.K. Castellano, F. Diederich, Interactions with aromatic rings in chemical and biological recognition, Angew. Chem. Int. Ed. 42 (2003) 1210–1250.
[6] M.W. Gonzalez, M.G. Kann, Chapter 4: protein interactions and disease, PLoS Comput. Biol. 8 (2012), e1002819-e1002819. .
[7] J.R. Kenny, M.M. Liu, A.T. Chow, J.C. Earp, R. Evers, J.G. Slatter, D.D. Wang, L. Zhang, H. Zhou, Therapeutic protein drug-drug interactions: navigating the knowledge gaps-highlights from the 2012 AAPS NBC Roundtable and IQ Consortium/FDA workshop, AAPS J. 15 (2013) 933–940.
[8] L. Di, C. Breen, R. Chambers, S.T. Eckley, R. Fricke, A. Ghosh, P. Harradine, J.C. Kalvass, S. Ho, C.A. Lee, P. Marathe, E.J. Perkins, M. Qian, S. Tse, Z. Yan, M.J. Zamek-Gliszczynski, Industry perspective on contemporary protein-binding methodologies: considerations for regulatory drug-drug interaction and related guidelines on highly bound drugs, J. Pharm. Sci. 106 (2017) 3442–3452.
[9] A. Bratek-Skicki, P. Żeliszewska, J.M. Ruso, Fibrinogen: a journey into biotechnology, Soft Matter 12 (2016) 8639–8653.
[10] M.P. De Maat, Effects of diet, drugs, and genes on plasma fibrinogen levels, Ann. N. Y. Acad. Sci. 936 (2001) 509–521.
[11] A. Lodi, A. Saha, X. Lu, B. Wang, E. Sentandreu, M. Collins, M.G. Kolonin, J. DiGiovanni, S. Tiziani, Combinatorial treatment with natural compounds in prostate cancer inhibits prostate tumor growth and leads to key modulations of cancer cell metabolism, npj Precision Oncology 1 (2017) 18.
[12] M.H.M. Leung, T.W. Kee, Effective stabilization of curcumin by association to plasma proteins: human serum albumin and fibrinogen, Langmuir 25 (2009) 5773–5777.
[13] V.V. Kleandrova, F. Luan, H. González-Díaz, J.M. Ruso, A. Melo, A. Speck-Planche, M.N.D. Cordeiro, Computational ecotoxicology: simultaneous prediction of ecotoxic effects of nanoparticles under different experimental conditions, Environ. Int. 73 (2014) 288–294.
[14] Z.J. Deng, M. Liang, I. Toth, M.J. Monteiro, R.F. Minchin, Molecular interaction of poly (acrylic acid) gold nanoparticles with human fibrinogen, ACS Nano 6 (2012) 8962–8969.
[15] Y. Liu, X. Tang, J. Pei, L. Zhang, F. Liu, K.a. Li, Gastrodin interaction with human fibrinogen: anticoagulant effects and binding studies, Chem. Eur. J. 12 (2006) 7807–7815.

[16] N. Hassan, P. Verdes, J.M. Ruso, Assessment of interactions between four proteins and benzothiazole derivatives by DSC and CD, J. Chem. Thermodyn. 43 (2011) 399–404.
[17] M. Subramanyam, R. Sreenivasulu, R. Gundla, M.V. Rao, K.P. Rao, Synthesis, biological evaluation and docking studies of 1, 3, 4-oxadiazole fused benzothiazole derivatives for anticancer drugs, Letters in Drug Design & Discovery 15 (2018) 1299–1307.
[18] R.S. Keri, M.R. Patil, S.A. Patil, S. Budagumpi, A comprehensive review in current developments of benzothiazole-based molecules in medicinal chemistry, Eur. J. Med. Chem. 89 (2015) 207–251.
[19] D.C. Henry, A. Lapworth, The cataphoresis of suspended particles. Part I.— the equation of cataphoresis, Proceedings of the Royal Society of London. Series A, Containing Papers of a Mathematical and Physical Character 133 (1931) 106–129.
[20] J.G. Greener, M.J.E. Sternberg, AlloPred: prediction of allosteric pockets on proteins using normal mode perturbation analysis, BMC bioinformatics 16 (2015) 335.
[21] D.E. Mager, D.R. Abernethy, Use of wavelet and fast fourier transforms in pharmacodynamics, J. Pharmacol. Exp. Ther. 321 (2007) 423–430.
[22] K. Odziomek, D. Ushizima, P. Oberbek, K.J. Kurzydłowski, T. Puzyn, M. Haranczyk, Scanning electron microscopy image representativeness: morphological data on nanoparticles, J. Microsc. 265 (2017) 34–50.
[23] T. Wiseman, S. Williston, J.F. Brandts, L.-N. Lin, Rapid measurement of binding constants and heats of binding using a new titration calorimeter, Anal. Biochem. 179 (1989) 131–137.
[24] S. Preus, K. Kilså, F.-A. Miannay, B. Albinsson, L.M. Wilhelmsson, FRETmatrix: a general methodology for the simulation and analysis of FRET in nucleic acids, Nucleic Acids Res. 41 (2013) e18.
[25] S. Preus, DecayFit—fluorescence decay analysis software 1.3, fluortools, http://www.fluortools.com 2014.
[26] N. Hassan, M.P. Gárate, T. Sandoval, L. Espinoza, Á. Piñeiro, J.M. Ruso, On the self-assembly of a highly selective benzothiazole-based TIM inhibitor in aqueous solution, Langmuir 26 (2010) 16681–16689.
[27] L.R. Barbosa, M.G. Ortore, F. Spinozzi, P. Mariani, S. Bernstorff, R. Itri, The importance of protein-protein interactions on the pH-induced conformational changes of bovine serum albumin: a small-angle X-ray scattering study, Biophys. J. 98 (2010) 147–157.
[28] J.M. Kollman, L. Pandi, M.R. Sawaya, M. Riley, R.F. Doolittle, Crystal structure of human fibrinogen, Biochemistry 48 (2009) 3877–3886.
[29] M. González-Durruthy, G. Scanavachi, R. Rial, Z. Liu, M.N.D.S. Cordeiro, R. Itri, J.M. Ruso, Structural and energetic evolution of fibrinogen toward to the betablocker interactions, Int. J. Biol. Macromol. 137 (2019) 405–419.
[30] R. Itri, L.Q. Amaral, Distance distribution function of sodium dodecyl-sulfate micelles by X-ray-scattering, J Phys Chem-Us 95 (1991) 423–427.
[31] D. Franke, M.V. Petoukhov, P.V. Konarev, A. Panjkovich, A. Tuukkanen, H.D.T. Mertens, A.G. Kikhney, N.R. Hajizadeh, J.M. Franklin, C.M. Jeffries, D.I. Svergun, ATSAS 2.8: a comprehensive data analysis suite for small-angle scattering from macromolecular solutions, J. Appl. Crystallogr. 50 (2017) 1212–1225.
[32] H.M. Berman, J. Westbrook, Z. Feng, G. Gilliland, T.N. Bhat, H. Weissig, I.N. Shindyalov, P.E. Bourne, The protein data bank, Nucleic Acids Res. 28 (2000) 235–242.
[33] O. Trott, A.J. Olson, AutoDock Vina: improving the speed and accuracy of docking with a new scoring function, efficient optimization, and multithreading, J. Comput. Chem. 31 (2010) 455–461.
[34] S. Forli, R. Huey, M.E. Pique, M.F. Sanner, D.S. Goodsell, A.J. Olson, Computational protein–ligand docking and virtual drug screening with the AutoDock suite, Nat. Protoc. 11 (2016) 905.
[35] S. Kim, P.A. Thiessen, E.E. Bolton, J. Chen, G. Fu, A. Gindulyte, L. Han, J. He, S. He, B.A. Shoemaker, PubChem substance and compound databases, Nucleic Acids Res. 44 (2015) D1202–D1213.
[36] J. Jiménez, S. Doerr, G. Martínez-Rosell, A. Rose, G. De Fabritiis, DeepSite: protein-binding site predictor using 3D-convolutional neural networks, Bioinformatics 33 (2017) 3036–3042.
[37] A. Tao, Y. Huang, Y. Shinohara, M.L. Caylor, S. Pashikanti, D. Xu, ezCADD: a rapid 2D/3D visualization-enabled web modeling environment for democratizing computer-aided drug design, J. Chem. Inf. Model. 59 (2018) 18–24.
[38] R. Thomsen, M.H. Christensen, MolDock: a new technique for high-accuracy molecular docking, J. Med. Chem. 49 (2006) 3315–3321.
[39] W.P. Feinstein, M. Brylinski, Calculating an optimal box size for ligand docking and virtual screening against experimental and predicted binding pockets, Journal of cheminformatics 7 (2015) 18.
[40] R.A. Laskowski, M.B. Swindells, LigPlot+: multiple ligand–protein interaction diagrams for drug discovery, ACS Publications 51 (10) (2011) 2778–2786.
[41] U. Emekli, D. Schneidman-Duhovny, H.J. Wolfson, R. Nussinov, T. Haliloglu, HingeProt: automated prediction of hinges in protein structures, Proteins: Structure, Function, and Bioinformatics 70 (2008) 1219–1227.
[42] W. Zheng, S. Doniach, A comparative study of motor-protein motions by using a simple elastic-network model, Proc. Natl. Acad. Sci. 100 (2003) 13253–13258.
[43] D. Ming, M.E. Wall, Allostery in a coarse-grained model of protein dynamics, Phys. Rev. Lett. 95 (2005), 198103. .
[44] J. de Ruyck, G. Brysbaert, R. Blossey, M.F. Lensink, Molecular docking as a popular tool in drug design, an in silico travel, Advances and applications in bioinformatics and chemistry: AABC 9 (2016) 1.
[45] J. Li, Q. Du, C. Sun, An improved box-counting method for image fractal dimension estimation, Pattern Recogn. 42 (2009) 2460–2469.
[46] M. Alia, A. Samsudin, New key exchange protocol based on Mandelbrot and Julia fractal set, International journal of computer science and network security 7 (2007) 302–307.
[47] Y. Fisher, Fractal Image Compression: Theory and Application, Springer Science & Business Media, Place Published, 2012.
[48] B.B. Mandelbrot, Plane DLA is not self-similar; is it a fractal that becomes increasingly compact as it grows? Physica A: Statistical Mechanics and its Applications 191 (1992) 95–107.
[49] B.B. Mandelbrot, Fractal aspects of the iteration of z→ Λz (1-z) for complex Λ and z, Ann. N. Y. Acad. Sci. 357 (1980) 249–259.
[50] D. Saupe, Efficient computation of Julia sets and their fractal dimension, Physica D: Nonlinear Phenomena 28 (1987) 358–370.
[51] J. Soddell, R. Seviour, Using box counting techniques for measuring shape of colonies of filamentous micro-organisms, Complex. Int. 2 (1995) 1–8.
[52] M. Nezadal, O. Zemeskal, M. Buchnicek, The Box-counting: Critical Study, 4th Conference on Prediction, Synergetic and More, The Faculty of Management, Institute of Information Technologies, Faculty of Technology, Tomas Bata University in Zlin, HarFA software, October, 2001 25–26.
[53] E. Ahmad, G. Rabbani, N. Zaidi, S. Singh, M. Rehan, M.M. Khan, S.K. Rahman, Z. Quadri, M. Shadab, M.T. Ashraf, Stereo-selectivity of human serum albumin to enantiomeric and isoelectronic pollutants dissected by spectroscopy, calorimetry and bioinformatics, PLoS One 6 (2011).
[54] E. Ahmad, G. Rabbani, N. Zaidi, B. Ahmad, R.H. Khan, Pollutant-induced modulation in conformation and β-lactamase activity of human serum albumin, PLoS One 7 (2012).
[55] N. Sturm, J.r.m. Desaphy, R.J. Quinn, D. Rognan, E. Kellenberger, Structural insights into the molecular basis of the ligand promiscuity, J. Chem. Inf. Model. 52 (2012) 2410–2421.
[56] A.M. Afzal, H.Y. Mussa, R.E. Turner, A. Bender, R.C. Glen, A multi-label approach to target prediction taking ligand promiscuity into account, Journal of cheminformatics 7 (2015) 24.
[57] P. Källblad, R.L. Mancera, N.P. Todorov, Assessment of multiple binding modes in ligand— protein docking, J. Med. Chem. 47 (2004) 3334–3337.
[58] C. Chennubhotla, A. Rader, L.-W. Yang, I. Bahar, Elastic network models for understanding biomolecular machinery: from enzymes to supramolecular assemblies, Phys. Biol. 2 (2005) S173.
[59] B.H. Lee, S. Seo, M.H. Kim, Y. Kim, S. Jo, M.-k. Choi, H. Lee, J.B. Choi, M.K. Kim, Normal mode-guided transition pathway generation in proteins, PLoS One 12 (2017) e0185658.
[60] T. Oliwa, Y. Shen, cNMA: a framework of encounter complex-based normal mode analysis to model conformational changes in protein interactions, Bioinformatics 31 (2015) i151–i160.
[61] O. Keskin, S.R. Durell, I. Bahar, R.L. Jernigan, D.G. Covell, Relating molecular flexibility to function: a case study of tubulin, Biophys. J. 83 (2002) 663–680.
[62] R.C. Gonzalez, R.E. Woods, Digital image processing [M], Publishing house of, Electron. Ind. 141 (2002).
[63] A. Malliani, M. Pagani, F. Lombardi, S. Cerutti, Cardiovascular neural regulation explored in the frequency domain, Circulation 84 (1991) 482–492.
[64] J.L. Semmlow, Biosignal and Medical Image Processing, CRC press, Place Published, 2008.
[65] G. Weng, U.S. Bhalla, R. Iyengar, Complexity in biological signaling systems, Science 284 (1999) 92–96.
[66] H. Li, S. Chen, H. Zhao, Fractal structure and conformational entropy of protein chain, Int. J. Biol. Macromol. 12 (1990) 374–378.
[67] A.D. Koromyslova, A.O. Chugunov, R.G. Efremov, Deciphering fine molecular details of proteins' structure and function with a Protein Surface Topography (PST) method, J. Chem. Inf. Model. 54 (2014) 1189–1199.
[68] G. Rabbani, E. Ahmad, N. Zaidi, S. Fatima, R.H. Khan, pH-Induced molten globule state of Rhizopus niveus lipase is more resistant against thermal and chemical denaturation than its native state, Cell Biochem. Biophys. 62 (2012) 487–499.
[69] G. Rabbani, E. Ahmad, M.V. Khan, M.T. Ashraf, R. Bhat, R.H. Khan, Impact of structural stability of cold adapted Candida antarctica lipase B (CaLB): in relation to pH, chemical and thermal denaturation, RSC Adv. 5 (2015) 20115–20131.
[70] R. Huang, B.L.T. Lau, Biomolecule–nanoparticle interactions: elucidation of the thermodynamics by isothermal titration calorimetry, Biochim. Biophys. Acta Gen. Subj. 1860 (2016) 945–956.
[71] M. Amaral, D. Kokh, J. Bomke, A. Wegener, H. Buchstaller, H. Eggenweiler, P. Matias, C. Sirrenberg, R. Wade, M. Frech, Protein conformational flexibility modulates kinetics and thermodynamics of drug binding, Nat. Commun. 8 (2017) 2276.
[72] J.J. Ewbank, T.E. Creighton, Structural characterization of the disulfide folding intermediates of bovine. Alpha.-lactalbumin, Biochemistry 32 (1993) 3694–3707.
[73] G. Rabbani, M.H. Baig, E.J. Lee, W.-K. Cho, J.Y. Ma, I. Choi, Biophysical study on the interaction between eperisone hydrochloride and human serum albumin using spectroscopic, calorimetric, and molecular docking analyses, Mol. Pharm. 14 (2017) 1656–1665.
[74] G. Rabbani, M.H. Baig, A.T. Jan, E. Ju Lee, M.V. Khan, M. Zaman, A.-E. Farouk, R.H. Khan, I. Choi, Binding of erucic acid with human serum albumin using a spectroscopic and molecular docking study, Int. J. Biol. Macromol. 105 ((2017) 1572–1580.
[75] M.M. Lopez, D. Kosk-Kosicka, Spectroscopic analysis of halothane binding to the plasma membrane Ca 2+-ATPase, Biophys. J. 74 (1998) 974–980.
[76] G. Rabbani, E. Ahmad, N. Zaidi, R.H. Khan, pH-dependent conformational transitions in conalbumin (ovotransferrin), a metalloproteinase from hen egg white, Cell Biochem. Biophys. 61 (2011) 551–560.
[77] A. Sułkowska, Interaction of drugs with bovine and human serum albumin, J. Mol. Struct. 614 (2002) 227–232.
[78] G. Rabbani, E.J. Lee, K. Ahmad, M.H. Baig, I. Choi, Binding of tolperisone hydrochloride with human serum albumin: effects on the conformation, thermodynamics, and activity of HSA, Mol. Pharm. 15 (2018) 1445–1456.

[79] G. Rabbani, M.J. Khan, A. Ahmad, M.Y. Maskat, R.H. Khan, Effect of copper oxide nanoparticles on the conformation and activity of β-galactosidase, Colloids Surf B Biointerfaces 123 (2014) 96–105.
[80] B. Wieb van der Meer, D.M. van der Meer, S.S. Vogel, FRET - Förster Resonance Energy Transfer: From Theory to Applications, Place Published, 2013 63–104.
[81] S. Jang, M.D. Newton, R.J. Silbey, Multichromophoric Forster resonance energy transfer, Phys. Rev. Lett. 92 (2004), 218301. .
[82] J.R. Lakowicz, Principles of Fluorescence Spectroscopy, Kluwer Academic/Plenum, Place Published, 1999.
[83] Y.-Z. Zhang, N.-X. Zhang, A.-Q. Ren, J. Zhang, J. Dai, Y. Liu, Spectroscopic studies on the interaction of 2,4-dichlorophenol with bovine serum albumin, J. Solut. Chem. 39 (2010) 495–510.
[84] J. Zhang, X.-F. Dai, J.-Y. Huang, Resveratrol binding to fibrinogen and its biological implication, Food Biophysics 7 (2012) 35–42.
[85] G. Scanavachi, Y.R. Espinosa, J.S. Yoneda, R. Rial, J.M. Ruso, R. Itri, Aggregation features of partially unfolded bovine serum albumin modulated by hydrogenated and fluorinated surfactants: molecular dynamics insights and experimental approaches, J. Colloid Interface Sci. 572 (2020) 9–21.
[86] A. Guinier, G. Fournet, Small-Angle Scattering of X-rays, Wiley, Place Published, 1955.